IPP-Report

Max-Planck-Institut
für Plasmaphysik

Alexander Kendl

Drift wave instability and turbulence in advanced stallarator configurations

IPP 5/95
August 2001

Alexander Kendl

Drift wave instability and turbulence in advanced stallarator configurations

IPP 5/95
August 2001

Contents

Chapter 1

Prelude

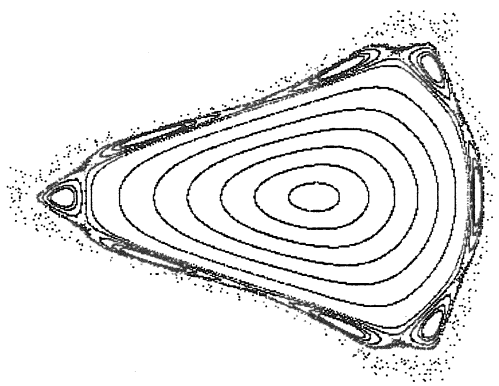

Ceci n'est pas un Stellarator

Small scale, low frequency fluctuations are generally held responsible for the observed transport losses in fusion plasmas that exceed single particle collisional transport by orders of magnitude. Experimental evidence suggests drift waves as a probable cause of the underlying instabilities [1]. The basic mechanism of instability for drift waves is independent of the confining magnetic field geometry: free energy from a pressure gradient together with a non-adiabatic interaction between ions and parallel electron dynamics leads to a nonlinear growth of wave amplitude. The coupling of different wave numbers results in a locally homogenous, quasi two-dimensional turbulent state on the typical perpendicular length scale of several ion gyro radii [2]. Stabilizing and catalyzing factors, like global and local shear damping or curvature of the magnetic field, are on the other hand fundamentally determined by the geometry of magnetic confinement. Different stellarator configurations are thus likely to also show specific anomalous transport behaviour. For advanced stellarators, this specifically accounts for the plasma edge, where measured turbulent transport exceeds the predicted neoclassical level by far [3]. In present partially optimized experiments the plasma core however is still dominated by collisional transport [3], but ion temperature gradient (ITG) driven core turbulence [4] might become significant in future devices with improved neoclassical confinement and higher core temperature.

It is thus desirable to put the understanding of the underlying microinstabilities in stellarators on a similarly solid foundation like it exists for large-scale magneto-hydrodynamic (MHD) stability. A well-known approach for the analysis of MHD stability of a plasma utilizes the energy principle. By means of a quadratic form, information

on destabilization, for example due to unfavourable curvature, and suitable geometric optimization in a stellarator can be obtained in this case [5].

Because of non-hermiticity in their governing equations, linear drift waves however do in general not allow for the construction of such a quadratic form. For the special case of a simple, collisionless model of radial drift waves, Antonsen [6] had been able to set up a quadratic stability criterion by extension of the real radial coordinate into the complex plane and rotation of the integration axis. This method has been extended by Chen *et al.* [7] for the case of dissipative drift waves, where it has been shown that those are linearly stable in a sheared slab configuration. In the formulation of the problem as an equation along the field line in order to cover toroidal and helical variations in general three-dimensional geometry, the trick of complex continuation is no longer practicable.

Further, the applicability of such a linear stability criterion on transport prediction would be questionable, as due to the nonlinear character of drift wave turbulence, even for linear stability of all eigenmodes, the formation of nonlinear self-sustained turbulence and thus enhanced transport is possible [8]. Simple analytical criteria for stabilization of drift waves in three-dimensional geometry thus can not be specified. For this reason we have chosen the approach of comparative numerical studies.

In the following chapter, an overview and references on the physics and geometry of helical advanced stellarators is given. On the basis of this configuration, the influence of magnetic field geometry is then discussed in a basic model of drift-Alfvén wave turbulence which contains the necessary physics that applies to the plasma edge (chapter 6). By means of linear models, core physics in the form of ITG (chapter 5) and dissipative trapped electron modes (chapter 4) is further included in our survey. These models are, of course, by far not comprehensive in order to cover the complex physics of plasma turbulence in three-dimensional fusion devices, where a large range of parameter and mode regimes is present. Optimization criteria for a possible systematic minimization of turbulent transport in Helias configurations therefore still have to be regarded as tentative. The results presented here should, however, encourage for more detailed future computations.

This report is based on the doctoral thesis "Driftwellen in Helias-Konfigurationen" by the same author presented to the Technical University of Munich in 2000. Parts of the contents have also been published in references [9], [10] and [11].

Chapter 2

Helias configurations

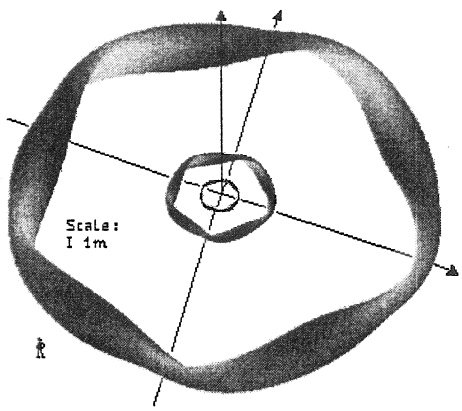

Size comparison of plasma volumes from Wendelstein 7-AS (inside), W7-X and the reactor concept HSR.

Helical advanced stellarator (Helias) configurations [12] find their foundations in the basic ideas of A. Schlüter aiming towards the goal of improving the confinement and equilibrium properties of a classical stellarator. The first experiment in this advanced line has been the partially optimized stellarator *Wendelstein 7-AS* [13], that has been in operation since 1988 and was able to succesfully demonstrate the feasibility of the concept [14, 15]. As next step (under construction), *Wendelstein 7-X* has been developed [16] to test the reactor relevance of Helias configurations. "HSR" (Helias stellarator reactor) is the name of a power plant concept study based on *W7-X* and scaled to reactor dimensions [17].

The basic properties of a Helias configuration are a MHD stable plasma with temperature T and density n up to a pressure, averaged over the whole plasma, of $\langle\beta\rangle = \langle 2\mu_0 nT/B^2\rangle \approx 5\%$ with low Shafranov shift due to reduction of Pfirsch-Schlüter currents, and low neoclassical losses [18]. Further criteria of optimization have been good confinement properties for α-particles, low bootstrap currents and well-defined magnetic surfaces of the vacuum field without major resonances [5, 19]. The currently favoured realization is a five field-period configuration (see figure 2.1) with rotational transform ι close to unity and low global shear.

2.1 Flux coordinates

In the following, straight-field line (SFL) Boozer or Hamada coordinates x^μ with

$$\mathbf{x} = (x^1, x^2, x^3) = (s, \theta, \zeta) \tag{2.1}$$

are used where s is the radial label and

$$\xi = (\zeta - q\theta) \tag{2.2}$$

is the field line label [20]. The magnetic field can then be written as

$$\mathbf{B}_0 = \nabla\xi \times \nabla\chi_p, \tag{2.3}$$

where $2\pi\chi_p$ is the poloidal flux and the safety factor is $q = \partial\Psi/\partial\chi_p = 1/\iota$. The radial coordinate s is defined via the flux derivative $\Psi_s' = B_0 a_0^2$ with B_0 the field strength on axis and average minor radius a_0. In our treatment of three-dimensional plasmas, all relevant geometrical quantities for a given configuration are represented in terms of metric elements

$$g^{\mu\nu} = \nabla x^\mu \cdot \nabla x^\nu. \tag{2.4}$$

Both ∇ and x^μ are normalized to the minor radius a_0. The geometric quantities are obtained by means of a free boundary equilibrium code (NEMEC) [21] and transformation to Boozer coordinates by the JMC code [22]. Cylindrical components $\mathbf{X} = (R, \phi, Z)$ of closed flux surfaces and the magnetic field are given as a function of SFL coordinates in a Fourier expansion in the mode numbers n and l ($N_f = 5$ is the number of field periods):

$$|B| = \sum_{n,l} B_{nl}(s)\cos(n\theta - l\zeta), \tag{2.5}$$

$$R = \sum_{n,l} R_{nl}(s)\cos(n\theta - l\zeta), \tag{2.6}$$

$$Z = \sum_{n,l} Z_{nl}(s)\sin(n\theta - l\zeta), \tag{2.7}$$

$$\phi = \frac{\zeta}{N_f} + \frac{1}{N_f}\sum_{n,l} \phi_{nl}(s)\sin(n\theta - l\zeta) \tag{2.8}$$

From these the covariant basis vector

$$\mathbf{e}_\mu = \frac{\partial \mathbf{X}}{\partial x^\mu} \tag{2.9}$$

and, in succession, the contravariant basis vectors

$$\mathbf{e}^\mu = \nabla x^\mu = \frac{(\mathbf{e}_\nu \times \mathbf{e}_\lambda)}{[\mathbf{e}_\mu \cdot (\mathbf{e}_\nu \times \mathbf{e}_\lambda)]} \tag{2.10}$$

are computed. The metric coefficients $g^{\mu\nu}$ are symmetric, and the non-diagonal elements vanish in an orthogonal coordinate system. The Jacobian of the transformation into the curvilinear coordinate system is $\hat{J} = [\hat{\nabla}s \cdot (\hat{\nabla}\theta \times \hat{\nabla}\zeta)]^{-1}$. The vector operator ∇ is written as

$$\nabla = \nabla u^i \frac{\partial}{\partial u^i}, \tag{2.11}$$

where a double occurrence of indices i implies a summation over its values (1,2,3).

Field line curvature is defined via the unit vector $\mathbf{b} = \mathbf{B}/B$ along the field line as

$$\boldsymbol{\kappa} \equiv \mathbf{b} \cdot \nabla \mathbf{b} = \frac{\mu_0}{B^2} \nabla_\perp \left(p + \frac{B^2}{2\mu_0} \right) \approx \nabla_\perp \ln B. \tag{2.12}$$

The second identity follows from the equilibrium relation $\nabla p = \mathbf{J} \times \mathbf{B} = \mu_0^{-1} (\nabla \times \mathbf{B}) \times \mathbf{B}$ directly by making use of some vector relations. The latter approximation is valid for low plasma pressure ($\beta \ll 1$). Then we have

$$\boldsymbol{\kappa} = \partial_s \ln B \cdot \nabla s + \partial_\theta \ln B \cdot \nabla \theta + \partial_\zeta \ln B \cdot \nabla \zeta. \tag{2.13}$$

Global field line shear $\Sigma = -(2s/\iota)\partial_s \iota$ describes the radial variation of the rotational transform. Helias configurations are characterized by low global shear. However, caused by deformation of the flux surfaces, radially neighbouring field lines may shear apart locally and get closer at other places even when the average (global) shear vanishes. A corresponding local description can be found by defining (see Ref. [23])

$$\mathbf{Q} = \frac{\nabla \chi \times \mathbf{B}}{|\nabla \chi|^2}, \tag{2.14}$$

and thus $\mathbf{B} = \mathbf{Q} \times \nabla \chi$. It is further $\mathbf{Q} = \nabla \xi - \Lambda \nabla \chi$, where

$$\Lambda \equiv \frac{\nabla \chi \cdot \nabla \xi}{|\nabla \chi|^2} = -(R + \frac{\partial q}{\partial \chi} \theta) \quad \text{with} \quad R = -(\nabla \chi \cdot \nabla \zeta - q \nabla \chi \cdot \nabla \theta)/|\nabla \chi|^2 \tag{2.15}$$

is often called integrated local shear. This secular quantity is depending on a point of reference along the field line and grows nonperiodically proportional to θ after a circuit around the torus. R is termed integrated residual shear. *Local shear* S now can be defined as quantity that is equal to global shear $\Sigma = \langle S \rangle_\Psi$ when averaged over a complete flux surface. The usual definition is [23]

$$S \equiv -\mathbf{B} \cdot \nabla \Lambda. \tag{2.16}$$

This is identical to $S = -\mathbf{Q} \cdot \mathrm{rot}\mathbf{Q}$ and has the dimension of an inverse volume.

For further reading, the most comprehensive treatment of flux coordinate systems can be found in the text book by D'haeseleer *et al.* [20].

2.2 Anomalous transport in stellarator geometry

The connection of a drift-optimized Helias stellarator geometry with anomalous transport has previously been discussed analytically with regard to the effect of fixed, prescribed fluctuations of electric and magnetic fields on fluxes by Wobig [5]. It is shown therein that in such a case fluctuation induced particle transport in a Helias has no direct dependence on the geometric properties of an optimized, low geodesic curvature configuration. The anomalous heat flux has been found to include a term proportional to the minimized Pfirsch-Schlüter factor $(\mathbf{e}_p \cdot \mathbf{b})$, where $\mathbf{e}_p = \nabla\zeta \times \nabla s$ and $\mathbf{b} = \mathbf{B}/B$. It had been concluded that the geometry could instead enter directly into transport via the fluctuation level. Recently, the long-time behaviour of drift wave test particles orbits and transport in Helias configurations has been investigated by means of the mapping technique [24]. This mapping method allows to study the influence of magnetic islands on the transport, but also needs as input pre-calculated electrostatic and magnetic field perturbations. In that sense such calculations are not self-consistent, as the particle motion does not act back on the perturbed electromagnetic fields. In contrast to these previous considerations, we will outline in chapter 5 self-consistent first-principle direct numerical computations of turbulent fluctuations and transport in Helias geometry.

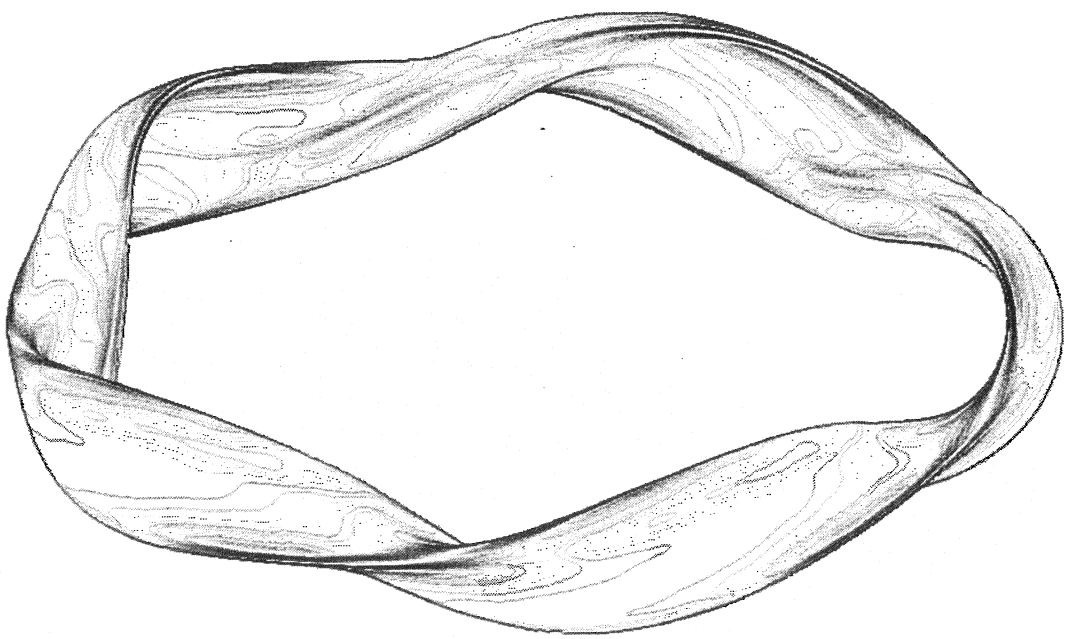

Figure 2.1. *Local shear contours on a flux surface of the Helias configuration Wendelstein 7-X. Notice the strong increase of local shear at regions of strong flux surface deformation, for example at the vertices of the triangular cross section parts.*

Chapter 3

Drift waves in inhomogenous plasma

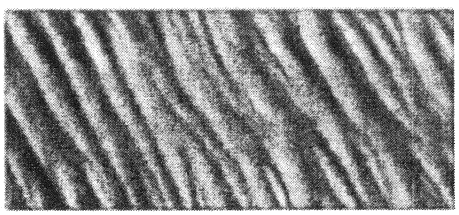

Measured density fluctuations generated by weakly turbulent drift weaves. From Ref. [25].

Collective phenomena in plasmas are most often described in the framework of magneto hydrodynamics (MHD) [26]. The use of the approximations employed in this model is justified when background scales lengths and mode structures are large compared to the parallel mean free path and to the gyro radius, and when other kinetic effects like Landau damping can be neglected.

Fluid equations are derived starting from the kinetic description of a plasma by taking moments of the distribution function $f(\mathbf{x}, \mathbf{v})$. In lowest order density, velocity and temperature of a fluid element are obtained:

$$n = \int d^3v f, \tag{3.1}$$

$$\mathbf{V} = (1/n) \int d^3v f \mathbf{v}, \tag{3.2}$$

$$T = (m/3n) \int d^3v f (\mathbf{v} - \mathbf{V})^2. \tag{3.3}$$

Under the assumptions mentioned above the distribution locally does not deviate much from a Maxwellian, and the (in principle infinite) hierarchy may be closed after these first three moments. The resulting fluid description is determined by the equations for conservation of density, momentum and energy. Ideal MHD uses single fluid equations without resistivity where all plasma components have the same density n, velocity $\mathbf{v}$ and temperature T. This most simplified model allows already for a description of the global equilibrium, the excitation of basic modes (sound waves, Alfvén waves) and their macroscopic stability [27].

A large class of instabilities is however not covered by this idealized approach and can be made accessible only when separate electron and ion dynamics and coupling via resistivity are additionally taken into account.

3.1 Fluid equations and drift ordering

The dynamics of a plasma is often paradigmatically described in the fluid model by means of the *Braginskii equations* [28] consisting of the equations of continuity and of conservation for momentum and energy of both species (index j):

$$\partial_t n_j + \nabla \cdot (n_j \mathbf{v}_j) = 0, \tag{3.4}$$

$$m_j n_j D_t \mathbf{v}_j = q_j n_j (\mathbf{E} + \mathbf{v}_j \times \mathbf{B}) - \nabla p_j - \nabla \Pi_j + \mathbf{R}, \tag{3.5}$$

$$\frac{3}{2} n_j \partial_t T_j + p_j \nabla \cdot \mathbf{v}_j = -\nabla \cdot \mathbf{q}_j - \Pi_j \nabla \mathbf{v}_j + Q_j. \tag{3.6}$$

Here $D_t = \partial_t + \mathbf{v}_j \cdot \nabla$ is the total time derivative, $\mathbf{q}_j$ is the heat flux, Π is the nonscalar part of the pressure tensor, $\mathbf{R}$ describes momentum exchange by collisions, and Q_j is a energy exchange term, each in the form derived by Braginskii [26].

A simple closure of the equations can be obtained with an (adiabatic or isothermal) equation of state $p(T)$. They are further coupled to Maxwell's equations

$$\nabla \times \mathbf{B} = \mu_0 \sum_j \mathbf{j}_j + \mu_0 \epsilon_0 \partial_t \mathbf{E} \tag{3.7}$$

and

$$\nabla \times \mathbf{E} = -\partial_t \mathbf{B}. \tag{3.8}$$

If quasi neutrality is a valid assumption ($n_i = n_e$), then one of the equations (3.4) can be also written as $\nabla \cdot \mathbf{j} = 0$, that is, the current is free of divergence.

The Braginskii equations in the form (3.4)-(3.6) describe plasma dynamics in a broad range of time scales. For fluctuations relevant to turbulent transport in a fusion plasma, typical scales of frequency $\omega \ll \Omega_j$ are small compared to the gyro frequencies $\Omega_j = q_j B / m_j$. Their spatial extension $\Delta \ll L$ is much smaller than typical length scales L of the background equilibrium that is only weakly depending on time and space variations. Then the dynamics in the equation of motion (3.5) can be reduced to these relevant scales by application of *drift ordering* [29, 30]: A perturbation analysis is performed in the small parameter

$$\epsilon \equiv \frac{\rho_s}{L} \sim \frac{\omega}{\Omega_j} \sim \frac{\Delta}{L} \ll 1. \tag{3.9}$$

Further it is assumed that fluctuating quantities are also small in order of ϵ compared to their equilibrium values. In lowest order in ϵ we obtain from the perpendicular component of (3.5) the drift velocities

$$\mathbf{v}_{\perp i} = \mathbf{v}_E + \mathbf{v}_{Di} + \mathbf{v}_{pi} \tag{3.10}$$

and

$$\mathbf{v}_{\perp e} = \mathbf{v}_E + \mathbf{v}_{De}. \tag{3.11}$$

Here convection through $\mathbf{E} \times \mathbf{B}$ drift is described by

$$\mathbf{v}_E = \frac{1}{B^2}(\mathbf{E} \times \mathbf{B}). \tag{3.12}$$

The diamagnetic drift

$$\mathbf{v}_{Dj} = \frac{\mathbf{B} \times \nabla p_j}{q_j n_j B^2} \tag{3.13}$$

has different sign for electrons and ions because of their specific charge q_j, and

$$\mathbf{v}_{pi} = \frac{m_i}{eB^2} D_t \mathbf{E} \tag{3.14}$$

is the polarization drift of the ions that appears due to finite mass inertia. Although $\mathbf{v}_{pi}$ is an order in ϵ smaller than the other terms, it is kept as for the finite space charge it is the only term that does not vanish by taking the divergence at a homogenous magnetic field. For the electrons this term is negligible. In eq. (3.4) and (3.6) also $\mathbf{v}_j = \mathbf{b}v_{\|j} + \mathbf{v}_{\perp j}$ is substituted and drift ordering is applied [30, 29]. In the Ampere's law in (3.7) the displacement current can further be neglected at low frequencies and high electric conductivity.

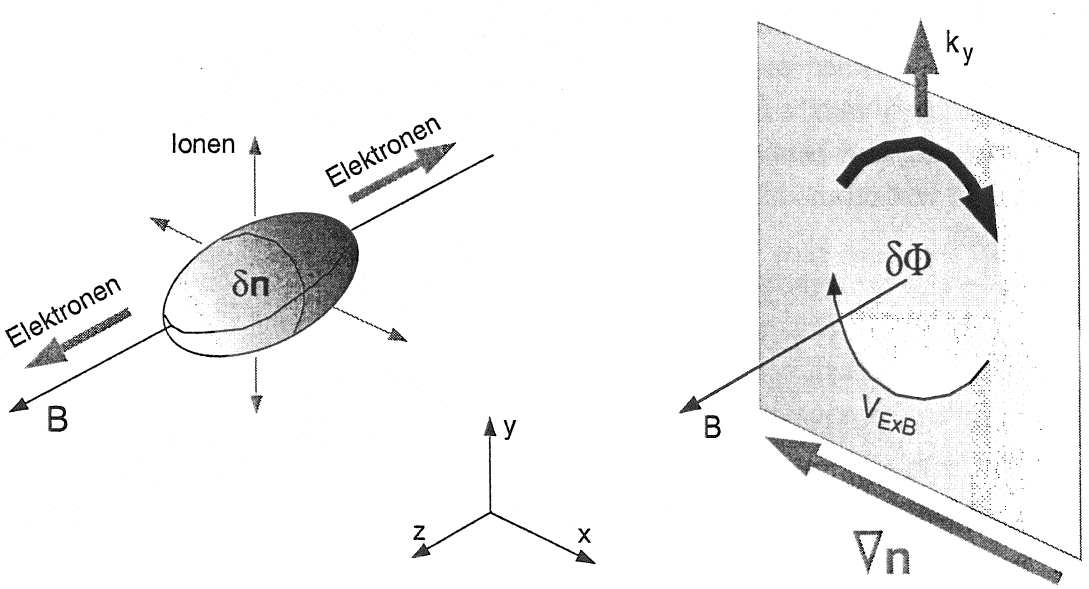

Figure 3.1. *Schematic view of a drift wave driven by a density gradient.*

3.2 Basic drift wave dynamics

The collective phenomena resulting from these drift reduced equations are often subsumed under the common term *drift waves*. On the other hand, drift waves in a narrow sense are often meant to designate the interrelated dynamics of perturbations in the pressure p and the electrostatic potential Φ subjected to a pressure gradient, where the perpendicular $\mathbf{E} \times \mathbf{B}$ motion carried by ions couples essentially to the parallel electron dynamics at finite $\nabla p_{e||}$ via the parallel component $j_{||}$ of the current [31, 32, 33]. The magnetic field may be homogenous. Drift waves are subject to a nonlinear character that enables self-sustained turbulence even without linear instability: Nonlinear advective coupling of $\mathbf{v}_E$ with vorticity $\nabla_\perp^2 \Phi$ opens more degrees of freedom for access on sources of free energy compared to linear perturbations, and thus may enable strong turbulence even if all linear modes are stable [34, 35, 8].

Destabilization occurs when the parallel electron dynamics deviates from a fast "adiabatic" response to potential perturbations [36]. Drift waves are a universal phenomenon that is found in magnetically confined plasma even for homogenous magnetic fields and cold ions. Figure 3.1 schematically shows a localized perturbation of ion density n_i (left) that results in a positive potential perturbation $\Phi > 0$ (right) due to ambipolar diffusion. The magnetic field is oriented in z direction. For typical scales Δ of the perturbation it is found that $\Delta \gg \lambda_D = \sqrt{\varepsilon_0 T_e/(ne^2)}$ is much larger than the Debye length, so that quasi neutrality $n_i \approx n_e$ can be assumed. Along the field line the electrons try to locally establish a Boltzmann relation $n_e = n_0(x) \exp(e\Phi/T_e)$ in accordance with their parallel equation of motion (3.5). Without restrictions on the parallel electron dynamics (like e.g. due to collisions, Alfvén waves or kinetic effects like Landau damping and particles trapped in magnetic field inhomogenities) this balance is established instantanously on the drift time scale and is often called an "adiabatic response" [36].

Already at homogenous background density the perturbation convects the plasma with $\mathbf{v}_\perp = \mathbf{v}_E$ due to the equal $\mathbf{E} \times \mathbf{B}$ drift for electrons and ions. By adding a density gradient in negative x direction, the whole structure propagates in y direction: It follows from the continuity equation (3.4) for a homogenous magnetic field and by neglecting ion inertia, that

$$\partial_t n_i + \nabla(\mathbf{v}_E\, n_i) = 0. \tag{3.15}$$

Using quasi neutrality $n_i{=}n_e{=}n_0(x){+}\tilde{n}_e$ and the stationary momentum balance

$$-en_0\mathbf{E}_{||} - \nabla_{||} p_e = 0 \tag{3.16}$$

for isothermal electrons without collisions, it follows that

$$n_i = n_0 \exp\left(\frac{e\Phi}{T_e}\right). \tag{3.17}$$

Combining equation (3.15) with the drift velocity $\mathbf{v}_E = B^{-2}(\mathbf{E}\times\mathbf{B}) = -B^{-2}(\nabla\Phi\times\mathbf{B})$ we now have

$$\partial_t\, n_0 \exp\left(\frac{e\Phi}{T_e}\right) - \nabla\left[\frac{1}{B^2}(\nabla\Phi\times\mathbf{B})\, n_0 \exp\left(\frac{e\Phi}{T_e}\right)\right] = 0, \tag{3.18}$$

and due to $B = B_z$ we obtain

$$\partial_t\Phi - \left(\frac{T_e}{eB}\right)(\partial_x \ln n_0)\,\partial_y\Phi = 0. \tag{3.19}$$

Assuming a perturbation periodical in y with $\Phi = \tilde{\Phi}\exp[-i\omega t + ik_y y]$, we find as a typical frequency the diamagnetic frequency of the electrons

$$\hat{\omega}_{*e} = \omega_{*e}\frac{a_0}{c_s} = \frac{\rho_s k_y}{L_n}. \tag{3.20}$$

Here the density gradient length $L_n = |a_0\nabla_x \ln n_0|^{-1}$ and a thermal ion gyro radius $\rho_s = \sqrt{m_i T_e}/(eB)$, determined at electron temperature, have been introduced. The motion of the structure perpendicular to magnetic field and density gradient is still stable and does so far not cause any transport in x direction.

The drift wave is destabilized only when a phase shift $\delta_{\mathbf{k}}$ between potential and density perturbation is introduced by "nonadiabatic" electron dynamcis

$$\tilde{n}_e = n_0(1 - i\delta_{\mathbf{k}})\,\frac{e\Phi}{T_e} \tag{3.21}$$

The imaginary term $i\delta_{\mathbf{k}}$ in general is an antihermitic operator and describes dissipation of the electrons, that causes the density perturbations to proceed the potential perturbations in y by slowing down the parallel equilibration. This leads to an exponential growth $\exp(\gamma_k t)$ with $\gamma_k \sim \delta_k\omega_k$, and may for the case of resistive drift modes be described approximately by $\delta_k \approx (\omega\nu_e/k_{||}c_e^2)$ [36].

In the following chapter a linear drift wave model for cold ions and isothermal electrons is applied to stellarator geometry by using two simple cases for $\delta_{\mathbf{k}}$. Parallel coupling by electron motion causes the parallel wave number of the drift modes to follow the scale $L_{||}$ of inhomogenities of the background magnetic field as $k_{||} \sim 1/L_{||}$ and implies a typical anisotropy of $k_{||} \ll k_\perp$. In toroidal geometry the drift waves couple to ion sound waves for finite $k_{||}$, which leads to an eigenmode structure along the field line. Interchange effects (see fig. 3.2) caused by an inhomogenous magnetic field can lead to a localization of the modes, for example on the outside of the torus.

Parallel electron motion also couples drift waves to shear Alfvén waves, which are parallely propagating perpendicular magnetic field perturbations. With the vector potential $A_{||}$ as a further dynamic variable, the parallel electric field $E_{||}$, parallel electron motion, and nonlinearly the parallel gradient are modified [37]. The resulting equations are discussed in chapter 6 in the context of nonlinear simulations of drift-Alfvén turbulence.

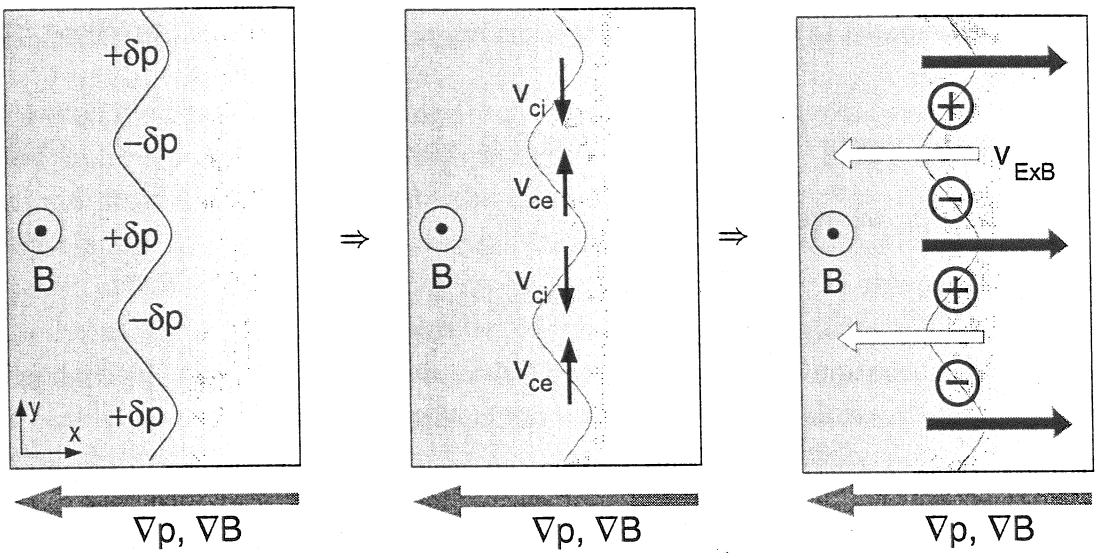

Figure 3.2. *Schematic view of the interchange instability in an inhomogenous plasma: an initial perturbation of pressure $p(x)$ with $\delta p = \delta p_0 \exp(iky)$ and a resulting $\mathbf{E} \times \mathbf{B}$ convection can be destabilized by diamagnetic currents for equally oriented gradients $\nabla B \cdot \nabla p > 0$. The drifts $\mathbf{v}_{cj} = (2p_j/q_j n_j B^2)\mathbf{B} \times \nabla \ln B$ correspond to the essential term of $\mathbf{v}_{Dj}$ that does not vanish when taking the divergence. Here the phase shift between pressure and potential is $\pi/2$.*

A destabilization of ion sound waves can be found for a finite ion temperature gradient (ITG) $\nabla_x T_i$ even at homogenous magnetic field and homogenous equilibrium density, when the parallel motion and perpendicular drift wave dynamics couple via parallel compressibility [38]. The instability of this ITG mode is increased by the ∇B drift for unfavourable curvature ($\nabla B \cdot \nabla p > 0$) of the field lines in toroidal geometry. ITG modes are commonly held responsible for transport in the low-collisionality core plasma [39], as this mechanism is already effective for adiabatic electrons. ITG modes in stellarator reactor geometry are discussed in chapter 5 in the framework of gyrokinetic theory.

Drift waves are stabilized by magnetic field line shear [40]. In a linear model, shear Σ causes a spatial dependence of $k_{||}$ across the field lines, what leads to an effective damping for localized eigenmodes with outgoing wave energy boundary conditions [7, 41, 36]. An absolute shear stabilization of dissipative drift modes, that had been found for constant magnetic field, does not occur any more in a torus with finite field line curvature[41]. Concerning a damping mechanism in globally nearly shearless stellarators, Waltz and Boozer have proposed in 1993 that local shear S may be an effective substitute [42]. In the following chapter, a numerical investigation on localization and stabilization of drift waves in Helias stellarators is conducted.

3.3 Ballooning transformation

Eigenfunctions on a flux surface in a toroidal system have to fulfil double periodicity in the coordinates $\theta \in [0...2\pi]$ and $\zeta \in [0...2\pi]$. On the other hand, the dynamics of drift waves is coupled strongly along the field lines, and the development of eigenmodes is oriented in filaments along the field with a parallel wave number $k_{||} \ll k_\perp$. Making use of this asymmetry by means of the WKB method and splitting the eigenmode problem into a spatially slowly varying parallel and a strongly oscillating perpendicular component (e.g. with Fourier decomposition) is not directly compatible with periodicity constraints.

A modified WKB method, that is able to fulfil these requirements, has been introduced by Connor *et al.* [43] and was further developed by Dewar and Glasser [45] for application to three-dimensional geometry. It allows to represent fluctuations in a quantity $\mathcal{F}$ with small amplitude by an eikonal ansatz with

$$\tilde{\mathcal{F}} = \mathcal{F}_\star(s,\zeta) \exp\left(\frac{i}{\varepsilon} W\right) \tag{3.22}$$

The eikonal $W = W(s,\xi)$ and amplitude $\mathcal{F}_\star(s,\zeta)$ are supposed to vary slowly on the scale of variations of the background quantities. The parallel coordinate is here represented by the toroidal angle ζ projected onto the field line. The eikonal depends on the radial coordinate s and field line label

$$\xi = \zeta - q\theta. \tag{3.23}$$

This fulfils the requirement

$$\mathbf{k}_\perp \cdot \mathbf{B} = 0 \tag{3.24}$$

by an ansatz

$$\mathbf{k}_\perp = \frac{1}{\varepsilon} \nabla W = k_\xi \nabla \xi + k_s \nabla s. \tag{3.25}$$

Here $k_\xi = \partial_\xi W$ and $k_s = \partial_s W$. Under the assumption of $W = \xi + \tilde{W}(s)$ and by defining a large perpendicular mode number $m = \varepsilon^{-1}$ and a radial wave number $\zeta_k = \varepsilon^{-1} \partial_s W / \partial_\xi W$ we can also write

$$\mathbf{k}_\perp = m \nabla \xi + \zeta_k \nabla s. \tag{3.26}$$

In lowest order in expansion by ε this ansatz reduces the eigenmode problem to the solution of a one dimensional equation along the field line, where m and ζ_k are free parameters.

The ballooning transformation by Connor et al. [43] translates these nonperiodic quasimodes from the infinite parallel domain back to a doubly periodic domain with periodic potential $\mathcal{F}_\star$ by summation in a series

$$\mathcal{F}_\star(s,\zeta) = \sum_{l=-\infty}^{+\infty} \mathcal{F}(s, \zeta + 2\pi l). \tag{3.27}$$

The quasimodes $\mathcal{F}$ now fulfil for decaying boundary conditions at $|\zeta| \to \infty$ the same equations as $\mathcal{F}_\star$. It has been noted by Antonsen and Lane [44] that this formulation still allows consistent treatment of local and global magnetic shear via the dependence of ∇W on these quantities along the field line.

The ballooning transformation had been developed initially for calculation of magneto hydrodynamic ballooning modes, and later it was also applied to drift waves. For MHD ballooning the formalism has also been extended to cover the radial mode structure by expansion to higher orders in ε [45]. Constructing global modes in three-dimensional stellarator geometry without axial symmetry by solution of ray tracing equations, that couple the eigenmodes along the field line for the free parameters ξ, s, k_ξ and k_s, is, however, not always generally practicable[1]. The resulting equations are in the form of a non-integrable four-dimensional Hamiltonian system, where even for small deviation from integrability KAM surfaces exist only in the axisymmetric case.

The quasimodes calculated in chapters 4 and 5 are thus only local approximations to actually global drift modes. The geometric properties of a stellarator are, however, still completely contained in these reduced equations. The WKB ansatz limits the treatment to small perpendicular wave lengths, which is justified by the scale of experimentally determined structures in the order of serveral gyro radii ρ_s for typical fusion plasmas. In toroidal and linear plasma devices with low temperature also drift modes with low mode number m are found, where this WKB approach is not any more applicable.

[1] R.L. Dewar, private communication

Chapter 4

Linear fluid theory: cold ion drift waves

It has been shown by Bhattacharjee *et al.* [46] that in linear helical symmetry electrostatic drift modes localize in helical ripple wells, and Waltz and Boozer [42] pointed out that these modes again should be effected by local ripple shear rather than global average shear. The eigenmode spectrum in linear helical symmetry has been studied by Persson *et al.* [47]. Little work, however, has been done on investigating drift modes in fully three-dimensional stellarator equilibria in the past, although the theory should in principle be a direct expansion of studies conducted in tokamak research.

At first Dominguez *et al.* [48] have calculated linear growth rates for the dissipative trapped electron mode in l=2 torsatrons in the ballooning mode formalism and found that, again, helically trapped particles have dominant influence on the stability in stellarators. Collisional drift waves in a three-period geometry have been discussed by Lewandowski through solving a linear fluid three-field model [49] and a gyrokinetic model [50, 51] as an initial-value problem along the field line and investigating the dependence of the growth rate on gradients and time. Recently, first results on construction of a global code for linear drift ballooning modes in general three-dimensional geometry have been presented by Kleiber [52].

In this chapter, we discuss in a simple electrostatic model the effect of stellarator optimization and local properties of shear and curvature on linear drift instability. A common feature of Helias stellarators is their intrinsic "shearlessness" with very weak global shear, which has led to the question of radial localization of drift modes. This was resolved in Ref. [42], where it has been shown that localization is determined by local shear from the helical ripple rather than by global average shear.

In this chapter we apply the most simple common model of electrostatic drift waves in the approximation of cold ions and quasi-adiabatic electron dynamics to general three-dimensional geometry. The Braginskii equations in the fluid model of a plasma are linearized with respect to the potential perturbation Φ: The continuity equation for ions

$$\partial_t n_i + \nabla \cdot (n_0 \mathbf{v}_i) = 0, \tag{4.1}$$

and the equation of motion for cold ions ($p_i = 0$)

$$-i\omega n_0 M \mathbf{v}_i = e n_0 \mathbf{E} + e n_0 (\mathbf{v}_i \times \mathbf{B}), \tag{4.2}$$

together with the linearized quasi neutrality condition

$$n_i \approx n_e = n_0 \left(1 + \xi_i \frac{e\Phi}{T_e}\right), \tag{4.3}$$

form a closed set of equations. The latter takes the place of the Poisson equation. Non-adiabaticity is represented by a phase $\xi_i = 1 - i\delta$ with $\delta > 0$. In the general case $\delta = \delta(\mathbf{k})$ is a function of the wave vector $\mathbf{k}$ [53]. For the rest of this chapter, δ is either assumed to be a constant parameter for simplicity, or is calculated perturbatively from the kinetic response of trapped electrons.

From the perpendicular and parallel components of the equation of motion (4.2) we obtain with $\mathbf{E} = -\nabla\Phi$ and $\nabla_{||} = \mathbf{b}(\mathbf{b} \cdot \nabla)$ the parallel velocity

$$\mathbf{v}_{||i} = \frac{1}{i\omega} \cdot \frac{e}{m_i} \nabla_{||} \Phi, \tag{4.4}$$

and, applying drift ordering, the perpendicular velocity

$$\mathbf{v}_{\perp i} = \mathbf{v}_E + \mathbf{v}_{pi}. \tag{4.5}$$

Here $\mathbf{v}_E = \frac{1}{B}\mathbf{b} \times \nabla_\perp \Phi$ is the $E \times B$ drift velocity and $\mathbf{v}_{pi} = -(e/m_i\Omega_s^2)\partial_t \nabla_\perp \Phi$ is the ion polarization velocity. $\Omega_s = c_s/\rho_s$ is the cyclotrone velocity, and $c_s = \sqrt{T_e/m_i}$ and $\rho_s = \sqrt{m_i T_e}/(eB)$ are, respectively, a sound velocity and a gyro radius of ions evaluated at electron temperature T_e.

Velocities (4.4), (4.5) are inserted into (4.1), which is linearized with respect to Φ:

$$-i\omega n_0 \xi \frac{e\Phi}{T_e} + \nabla \cdot (n_0 \mathbf{v}_E) + \nabla \cdot (n_0 \mathbf{v}_{pi}) + n_0 \nabla \cdot \mathbf{v}_{||i} = 0. \tag{4.6}$$

For that purpose the divergences are rewritten in linear approximation:

$$\nabla \cdot \mathbf{v}_E = \frac{1}{B}(\mathbf{b} \times \nabla \ln B) \cdot \nabla\Phi, \tag{4.7}$$

$$\nabla \cdot \mathbf{v}_{pi} = \frac{i\omega}{\Omega_s B} \nabla^2 \Phi, \tag{4.8}$$

$$\nabla \cdot \mathbf{v}_{||i} = \frac{e}{i\omega m_i} \nabla_{||}^2 \Phi, \tag{4.9}$$

When an eikonal representation in the context of the ballooning formalism is used for the perturbed potential (see previous chapter), we can write:

$$\Phi = \Phi(\zeta, s) \cdot \exp[-i\omega t + im\alpha], \tag{4.10}$$

Here $\alpha = \theta - \iota\zeta$ and m is the large perpendicular mode number. From (4.6-4.10) we thus obtain an ordinary second order differential equation for the electrostatic potential Φ:

$$\nabla_{\|}^2 \hat{\Phi} = U(\zeta, \omega)\hat{\Phi}. \tag{4.11}$$

The normalized complex potential $\hat{U} = a_0^2 U$ (also see [46, 42, 47, 48]) is defined by

$$\hat{U} = -\frac{\hat{\omega}}{\hat{B}}\left[\hat{\omega}\left(r_*^2 m^2 |\hat{\nabla}\alpha|^2 + \frac{\hat{B}\xi}{\hat{T}_e}\right) - r_* m(\mathbf{b} \times \hat{\nabla}\alpha) \cdot \hat{\boldsymbol{\kappa}}_\Delta\right]. \tag{4.12}$$

Here the dimensionless quantities $\hat{\Phi} \equiv e\Phi/T_{e0}$, $\hat{\nabla} \equiv a_0\nabla$, $\hat{T}_e \equiv T_e/T_{e0}$, $\hat{B} \equiv B/B_0$ and $\hat{\omega} \equiv \omega a_0/c_s$ have been introduced. T_{e0} is the electron temperature on axis, a_0 is the minor radius, and we abbreviate $\hat{\boldsymbol{\kappa}}_\Delta \equiv \hat{\nabla} \ln n_0 - \hat{\nabla} \ln B$. The magnetic field is written in the form $\mathbf{b} = \mathbf{B}/B = \hat{B}^{-1}(\hat{\nabla}s \times \hat{\nabla}\alpha)$.

By noting that $\xi_i = 1 - i\delta$ and $\hat{\omega} = \hat{\omega}_R + i\hat{\gamma}$ are both complex values we express $\hat{\Phi} = \hat{\Phi}_R + i\hat{\Phi}_I$, $\hat{U} = u_R + iu_I$, and finally obtain a set of two coupled ordinary differential equations:

$$F^2\partial_\zeta^2 \begin{pmatrix} \hat{\Phi}_R \\ \hat{\Phi}_I \end{pmatrix} = \begin{pmatrix} u_R & -u_I \\ u_I & u_R \end{pmatrix} \begin{pmatrix} \hat{\Phi}_R \\ \hat{\Phi}_I \end{pmatrix} \tag{4.13}$$

$F = 1/(\hat{B}\hat{J})$ is a metric factor where $\hat{J} = [\hat{\nabla}s \cdot (\hat{\nabla}\Theta \times \hat{\nabla}\zeta)]^{-1}$ is the Jacobian of the transformation to Boozer coordinates. We may now write Eq. 4.12 as

$$F^{-2}\hat{U} = -r\hat{\omega}\hat{J}^2\left[\hat{\omega}\left(\frac{\hat{B}^2\xi}{r\hat{T}_e} + rm^2\hat{B}\hat{K}\right) + \frac{m}{2}\left(\frac{\hat{B}^2}{L_n} - \hat{C}\right)\right], \tag{4.14}$$

The density scale length L_n is defined by $L_n^{-1} = \partial_s \ln n_0$. By using metric elements $g^{\mu\nu} = \nabla x^\mu \cdot \nabla x^\nu$ with $(x^\mu, x^\nu) \in (s, \theta, \zeta)$, we obtain

$$\hat{K} = g^{\alpha\alpha} = g^{ss}\left[\left(\frac{2\hat{B}}{g^{ss}}\right)^2 + \Lambda^2\right], \tag{4.15}$$

$$\hat{C} = g^{ss}\left[\left(\frac{2\hat{B}}{g^{ss}}\right)^2 \cdot \kappa_N + \Lambda \cdot \kappa_G\right]. \tag{4.16}$$

All metric elements $g^{\mu\nu}$ are periodic in ζ and secularity with respect to a localization point ζ_m arises through terms proportional to the global shear $\partial_s\iota$. We note that $\hat{K} \sim k_\perp^2$ is proportional to the square of the perpendicular wave vector. The secular quantity $\Lambda = g^{s\alpha}/g^{ss}$ is interpreted as the local shear $S = (\mathbf{b} \cdot \nabla)\Lambda$ integrated along the field

line [42]. We have introduced the notation $\kappa_N = \hat{\nabla} \ln \hat{B} \cdot \hat{\nabla} s = \sum_\mu g^{s\mu} \partial_\mu \ln \hat{B}$ for the normal curvature and $\kappa_G = \hat{\nabla} \ln \hat{B} \cdot (\hat{\nabla}\alpha - \Lambda \hat{\nabla} s)$ for the geodesic curvature. The magnetic field and all metrical quantities are calculated by using three-dimensional numerical equilibrium code data.

The system (4.13) of ordinary differential equations is solved using standard shooting techniques in a complex eigenvalue code for three-dimensional equilibria. Details of the numerical shooting and root finding procedures can be found elsewhere [47, 54]. Boundary conditions are found for a bordering point ζ_∞ sufficiently far outside from the localization region of square-integrable modes with [55]:

$$\hat{\Phi}_{\pm\zeta_\infty} = U^{-1/4} \cdot \exp\left[\pm \int_0^{\pm\zeta_\infty} d\zeta \sqrt{U}\right]. \tag{4.17}$$

For outgoing wave boundary conditions [40] we also use

$$\left.\frac{\mathrm{d}\hat{\Phi}}{\mathrm{d}\zeta}\right|_{\pm\zeta_\infty} = \left(\pm\sqrt{U} - \frac{1}{4U}\frac{\mathrm{d}U}{\mathrm{d}\zeta}\right)\hat{\Phi}. \tag{4.18}$$

All previous applications to stellarator-like configurations [47, 48] were restricted to symmetric modes only. We generalize this approach to arbitrary modes, as the most unstable mode may be found asymmetric and we will not be restricted to symmetric field lines. The frequency eigenvalues are thus now iterated until (complex) $\hat{\Phi}$ and its derivatives agree within a specified tolerance at a matching point ζ_m. The equations are solved on a grid along the field line with a resolution of 1000 points in ζ per one toroidal circuit (2π) by shooting from $\zeta_\infty = \zeta_m \pm 10 \cdot 2\pi$. For root finding a Mueller algorithm is used [56]. The starting points of the iteration are varied on a fixed grid in the frequency plane.

The Helias configurations are composed of 5 identical field periods with two symmetry planes in each period. A symmetry plane is a poloidal plane that shows both the fivefold toroidal rotational symmetry and simultaneously intersects a line of stellarator symmetry (see Ref. [57]). We define our magnetic coordinates in such a way as that the origin $\theta_0 = \zeta_0 = 0$ (and thus $\alpha = 0$) falls on the outboard side of the triangular shaped symmetry plane. The other (bean-shaped) plane of symmetry is at $\zeta_1 = \pi/5$. Along a field line passing through (θ_0, ζ_0) or (θ_0, ζ_1), an equilibrium quantity $f(\zeta)$ satisfies the symmetry $f(\zeta_{0,1} + \zeta) = f(\zeta_{0,1} - \zeta)$. As the solution of Eq. 4.13 along a given field line is independent of the matching point ζ_m, we may arbitrarily choose $\zeta_m = \zeta_0$. There remain two degree of freedom in the choice of α and radial label s, and to determine the most unstable mode of a configuration a scan over these parameters has to be performed.

4.1 Linear spectrum in "$i\delta$" approach

By solving Equations 4.13 for a given equilibrium we obtain the eigenfunctions and a spectrum of eigenvalues in the complex frequency plane (ω_R, γ). Non-square integrable eigenfunction solutions, as reported by Persson et al. [47], are ignored as unphysical and automatically suppressed. In this section we will limit our study to the one field line with label $\alpha = 0$, and focus on the dependence of solutions on geometrical properties local to this field line. We explicitly discuss the dependence on α and s later in section 4.4.

As matching point we take $\zeta_m = \zeta_0$ and we set s=1/4, which is halfway of the minor radius to the last closed flux surface on the outside of the torus. The density is assumed to have a bell shaped profile with $n = n_0(1-s)^q$ and $q \equiv 2$ where not explicitly stated otherwise, and temperature $\hat{T}_e(s = 1/4) \equiv 0.65$. For the non-adiabaticity, which can for example be due to collisions, we take the approach to assume an arbitrary fixed value of $\delta = 0.01$ (as e.g. in [47]). We will not investigate the dependence of the solution on this parameter but rather will later explicitly study the dissipative trapped electron mode in a perturbation ansatz. For the moment, we want to look at the influence of geometry only without the further complication due to particle trapping. For $\delta = 0$ all obtained solutions are marginally stable.

A typical frequency spectrum for W7-X obtained with $\delta = 0.01$ is shown in Fig. 4.1 for a mode number $m = 50$. Inset are real eigenfunctions Φ_R of this spectrum. In accordance with Refs. [46, 47, 48] we find with different choices of parameters both weakly and strongly localized modes. For each of the three Helias configurations such a spectrum is calculated for each perpendicular mode number m, and so the growth rate γ and real frequency ω_R of the most unstable solution (local to the specified field line) are obtained. In order not to mix geometry effects on the growth rate with artefacts due to blowing up of the device in scale, we have normalized the length scales to the respective minor radii of the devices. In Fig. 4.2 the three spectra are compared. The gyroratio parameter is set to $= 0.005$ identically for all configurations to the approximate value for W7-X.

The reduction of linear growth rate as shown here, from W7-AS to W7-X and HSR, may be understood when the local shear properties are examined. In Fig. 4.3 the local shear S has been plotted for all three configurations on the treated field line. The increase in the absolute value of S can be expected to have the major contribution to the observed favourable behaviour of one configuration over an other, since local shear is understood to play a considerable role in stabilizing drift waves [42]. An increase of S is only an indirect consequence of optimization: In the Helias approach to reduction of Pfirsch-Schlüter currents, helicity and field line torsion are increased in the stellarator. Through change of the pitch angle of field lines with radius, torsion again is related to shear S.

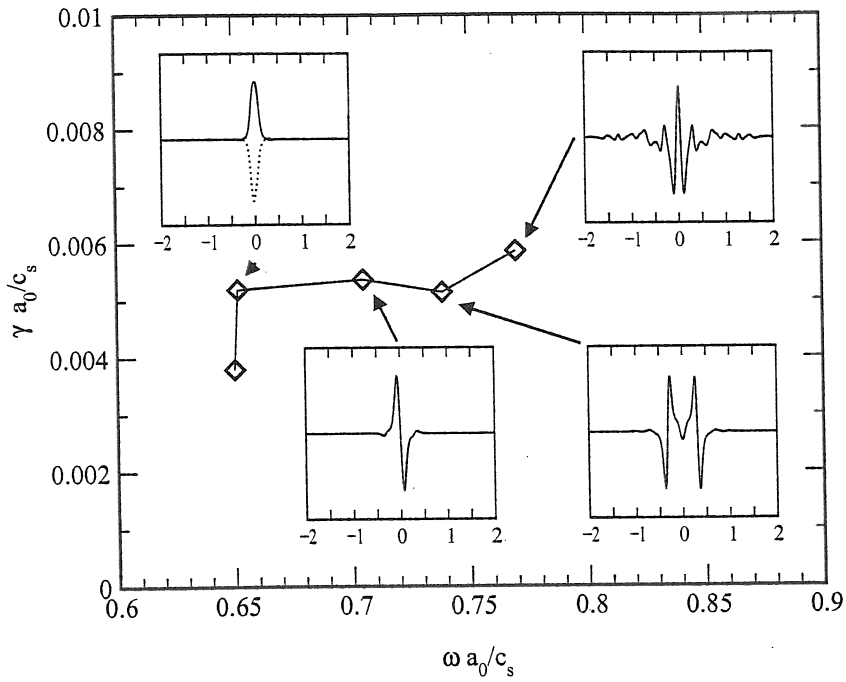

Figure 4.1. *Drift wave frequency spectrum and eigenfunctions for $m = 50$ and $\delta = 0.01$ in Wendelstein 7-X (s=1/4, α=0).*

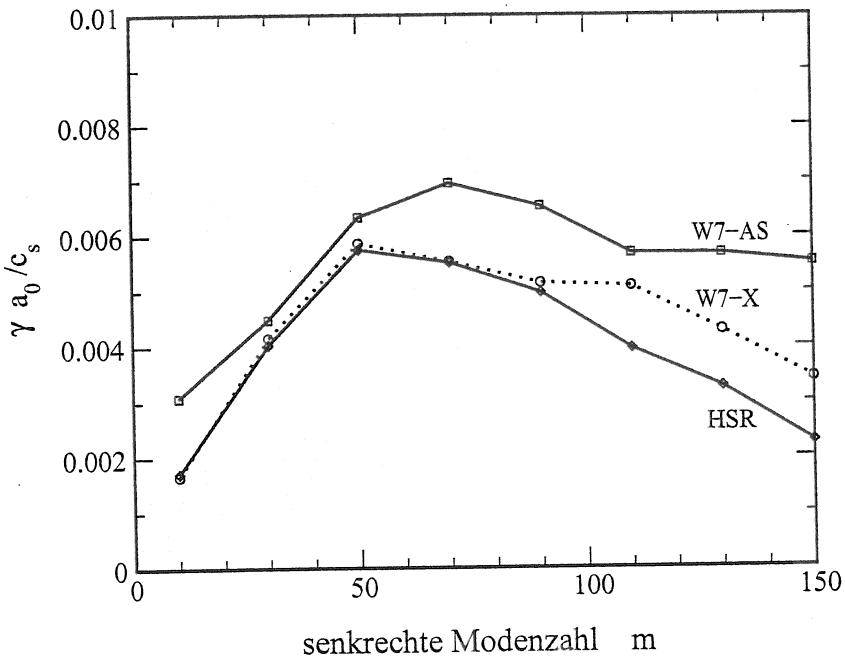

Figure 4.2. *Mode number spectra of various Helias configurations on α=0 field line for the $i\delta$-model.*

Still, HSR in Fig. 4.2 shows better performance for most mode numbers m despite less absolute local shear than W7-X. Besides local shear therefore other influences from geometry on stability and localization of modes have to be invoked. One more possible mechanism in the present ballooning type drift wave model is the overall favourable normalized normal curvature on the investigated field line for HSR, as shown (normalized as $\kappa_N/\sqrt{g^{ss}}$) in Fig. 4.4, compared to a substantial region with negative κ_N for W7-X (cf. Ref. [50]).

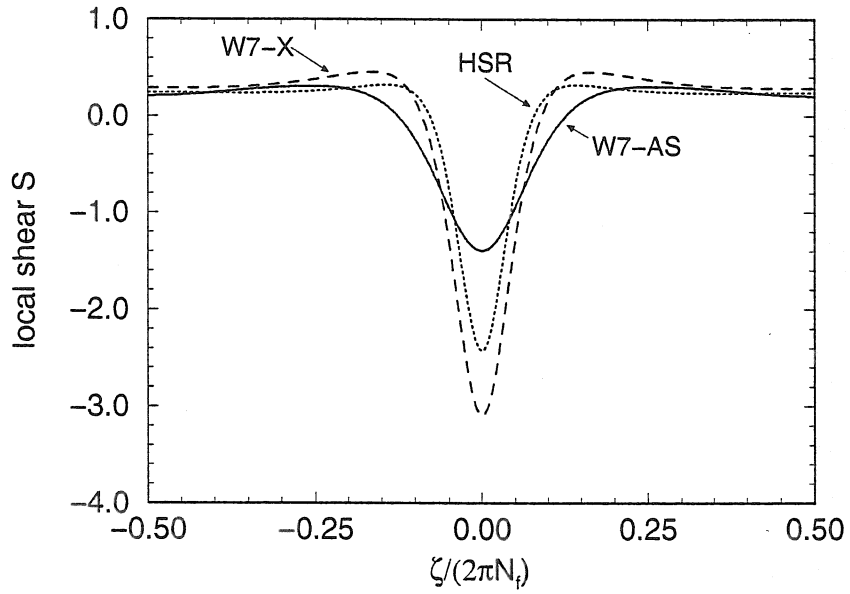

Figure 4.3. *Local shear S along the field line α=0 in one period on s=1/4 surface.*

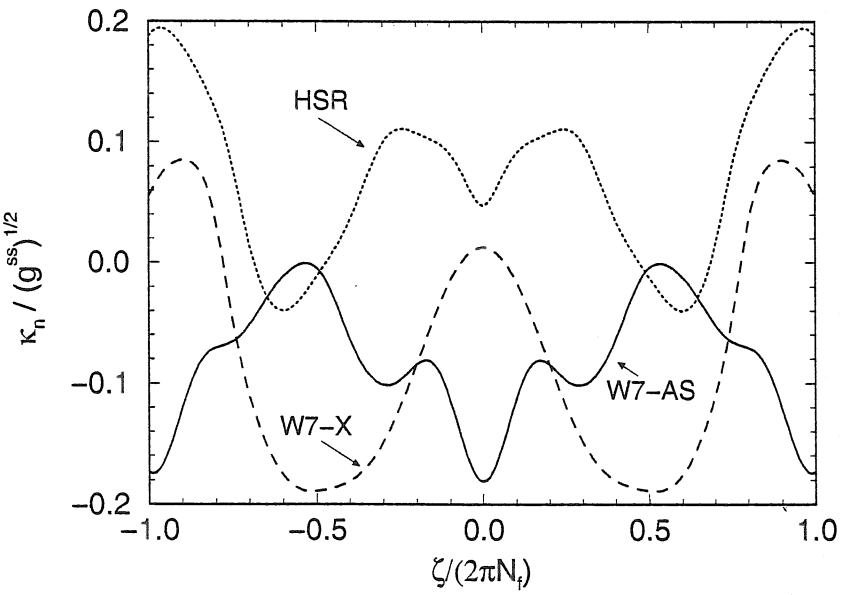

Figure 4.4. *Normal curvature κ_N: Along the treated field line HSR shows mostly favourable curvature.*

4.2 Trapped electron mode

Particles confined in a magnetic mirror can be detrapped by collisions, which is the cause for the trapped-particle instability. The effective collision frequency ν_{eff} is determined by the inverse time a particle needs to change its pitch angle through collisions in order to become untrapped. For electrons of energy E, $\nu_{\text{eff}} = (\nu_{ei}/\epsilon)(T_e/E)^{3/2}$ where $\sqrt{\epsilon}$ is the fraction of helically trapped electrons. The linear theory of the dissipative trapped electron mode (DTEM) has already been discussed by Dominguez *et al.* [48]. We basically follow this perturbative approach, and we thus arrive at

$$\hat{\nabla}_{||}^2 \hat{\Phi} = (\hat{U}_0 + \hat{U}_1)\hat{\Phi}. \tag{4.19}$$

Here $\hat{U}_0$ is real and correspondes to Eq. 4.12, and $\hat{U}_1 = i\hat{\omega}_0^2\delta$ is the complex perturbed part of the potential where δ is now calculated from trapped electron response. We will calculate $\Phi(\zeta)$ and the real eigenfrequencies ω_0 at first from the real equation $\hat{\nabla}_{||}^2\hat{\Phi} = \hat{U}_0\hat{\Phi}$, and perturbatively compute the complex change in the eigenfrequency to be

$$i\gamma = -\frac{\int \mathrm{d}\eta \Phi_0 U_1(\omega_0) \langle \Phi_0 \rangle}{\int \mathrm{d}\eta \Phi_0^2 \frac{\partial U_0}{\partial \omega}\Big|_{\omega_0}}, \tag{4.20}$$

In order to explicitly obtain $\hat{U}_1$, we start by assuming the nonadiabatic part g of the perturbed electron distribution function to be in the DTEM limit $\omega_b > \nu_{\text{eff}} > \omega$, where $\omega_b = v_{||}\mathbf{b}\cdot\nabla g$ is the bounce frequency of the trapped electrons [48]:

$$g(E,\mu) = \frac{iF_0}{\nu_{\text{eff}}}\left(\omega - \omega_*\left[1 + \eta_e\left(\frac{E}{T_e} - \frac{3}{2}\right)\right]\right)\left\langle\hat{\Phi}\right\rangle \equiv ig_0\left\langle\hat{\Phi}\right\rangle, \tag{4.21}$$

where F_0 is the electron equilibrium distribution function. Bounce average

$$\langle\hat{\Phi}\rangle = \frac{\int \mathrm{d}t_b \Phi}{\int \mathrm{d}t_b} \tag{4.22}$$

of the electrostatic potential perturbation is taken along the field line over the trapping region. The non-adiabatic part of the perturbed density

$$\frac{\tilde{n_1}}{n_0} = -i\delta\hat{\Phi} = 2\pi i \int \mathrm{d}v_{||} \int \mathrm{d}v_\perp v_\perp g_0 \langle\hat{\Phi}\rangle \tag{4.23}$$

is obtained by integration of g over velocity space. Contrary to the last chapter, δ now is no longer a constant but acts as an operator on $\langle\hat{\Phi}\rangle$. We explicitly evaluate δ by change in variables from

$$v_\perp = \sqrt{\frac{2}{m}\hat{B}E/\Lambda} \tag{4.24}$$

and

$$v_{||} = \sqrt{\frac{2E}{m}(1 - \hat{B}/\Lambda)} \tag{4.25}$$

to E and $\Lambda = E/\mu B$. Noting that $\nu_{\text{eff}} = \nu_{\text{eff}}^{(0)}(E/T)^{3/2}$, we can perform the integration over E:

$$\delta = \frac{2}{\sqrt{\pi}} \cdot \frac{\hat{\omega}_*^{(0)}}{\hat{\nu}_{\text{eff}}^{(0)}} \left[\left(1 - \frac{\hat{\omega}_0}{\hat{\omega}_*} \right) + \frac{3}{2}\eta_e \right] \cdot \int \frac{\mathrm{d}\Lambda/\Lambda^{3/2}}{\sqrt{\Lambda - \hat{B}}}. \tag{4.26}$$

The electron diamagnetic frequency is given by $\hat{\omega}_* = -2rm \cdot \partial_s \ln n_0 \hat{T}_e/\hat{B} \equiv r\hat{\omega}_*^{(0)}/\hat{B}$. With $\hat{U}_1$ as above and $\hat{U}_0 = \hat{U}(\xi = 1)$ we finally obtain

$$i\hat{\gamma} = \frac{2i}{\sqrt{\pi}} \frac{\hat{\omega}_0^2}{\hat{T}_e} \frac{\hat{\omega}_*^{(0)}}{\hat{\nu}_{\text{eff}}^{(0)}} \left[\frac{3}{2}\eta_e + \left(1 - \frac{\hat{\omega}_0}{\hat{\omega}_*} \right) \right] \cdot \frac{H_1}{H_2}, \tag{4.27}$$

$$H_1 = \sum_{\text{Interv}} \int \frac{\mathrm{d}\Lambda}{\Lambda^{3/2}} \frac{\left| \int \frac{\mathrm{d}\zeta}{F} \frac{\Phi_0(\zeta)}{\sqrt{\Lambda - \hat{B}(\zeta)}} \right|^2}{\left(\int \frac{\mathrm{d}\zeta}{F} \frac{1}{\sqrt{\Lambda - \hat{B}(\zeta)}} \right)},$$

$$H_2 = \int \frac{\mathrm{d}\zeta}{F\hat{B}} |\Phi_0|^2 \left[2\hat{\omega}_0 \left(rm^2 |\hat{\nabla}\alpha|^2 + \frac{\hat{B}}{r\hat{T}_e} \right) - m(\mathbf{b} \times \hat{\nabla}\alpha) \cdot \hat{\boldsymbol{\kappa}}_\Delta \right].$$

The integration over ζ along the field line is carried out between turning points, and that over the particle energy $\Lambda = E/(\mu B_0)$ between maximum values of B along the field line in one trapping interval; thus a factor of 2 difference in Eq. 4.27 to the corresponding equation in Ref. [48] (Note that some other minor differences arise e.g. from us explicitly taking into account the B-dependence of ρ_s). A summation has to be carried through in H_1 over all trapping intervals.

Again, we obtain a mode number spectrum for each of the three Helias devices. We set $\hat{\nu}_{\text{eff}} \equiv 0.2$ equally for all configurations. For W7-X and $m = 50$ the local frequency spectrum is shown in Fig. 4.5. The most unstable solutions (local to the field line in focus) for all investigated mode numbers m are compiled in Fig. 4.6. In addition to the role of local shear as previously discussed, now also the interplay between trapping intervalls and regions of good and bad magnetic field curvature comes to significance. Generally, in W7-X most particles are trapped in regions of favourable magnetic curvature. On the other hand, in W7-AS additional magnetic traps are created through coils that are located close by the plasma. For the specific field line of our choice (α=0, s=1/4) we plot the eigenfunctions of the electrostatic potential $\Phi(\zeta)$ against the magnetic field $\hat{B}$ for the most unstable $m = 50$ modes in Fig. 4.7. One can recognize the highly localized position in a single helical ripple of the W7-AS wave function in a region with the possibility of a variety of both helical and toroidal trapping zones. As has been pointed out in Ref. [48], the more localized a mode the more unstable it becomes. The basic modes of W7-X and HSR, on the other hand, show a delocalization to more helical wells.

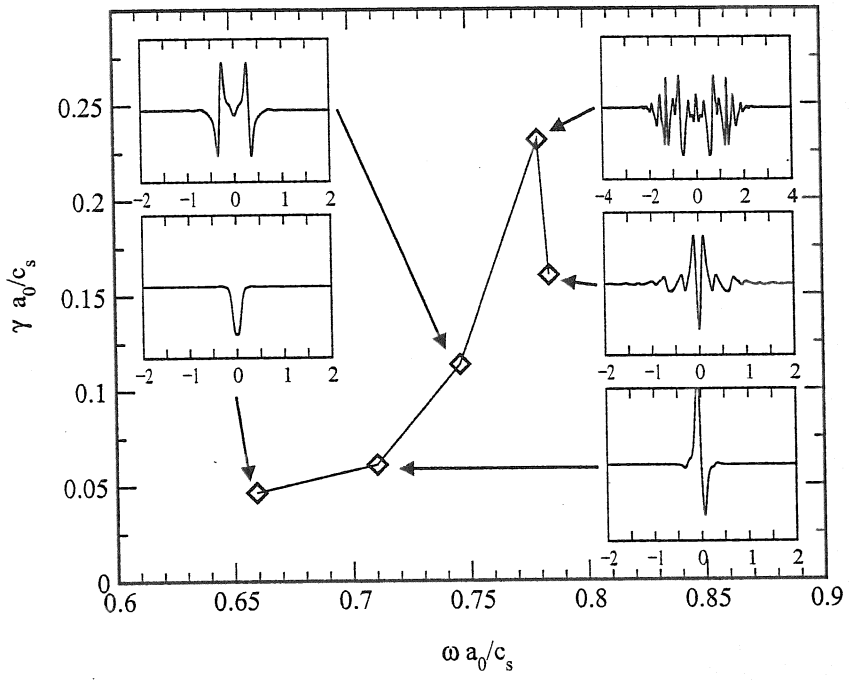

Figure 4.5. *DTEM frequency spectrum for W7-X ($m = 50$). Inset are wave functions Φ_R of some helically and toroidaly localized modes.*

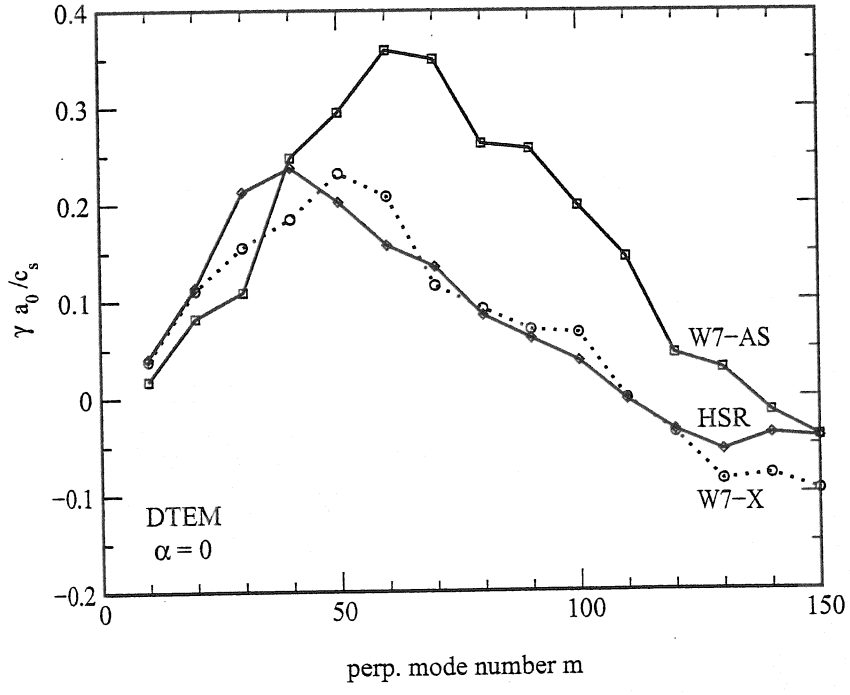

Figure 4.6. *DTEM mode number spectra for the same parameters as Fig. 4.*

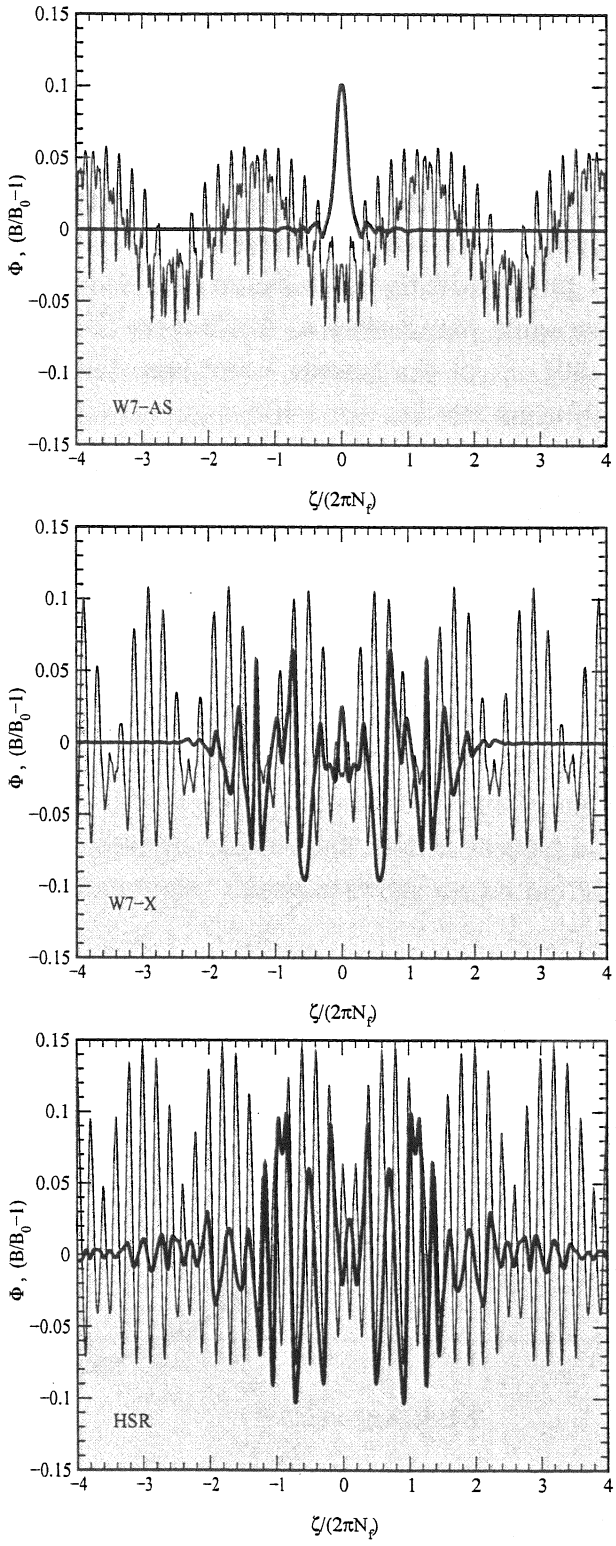

Figure 4.7. *For the same mode number ($m = 50$), W7-AS, W7-X and HSR (from top) show differently localized wave functions for the locally most unstable modes. Corresponding magnetic field strengths $\hat{B}$ are depicted shaded.*

4.3 The role of local shear

The results of the last two sections implied a crucial role of local shear and curvature for drift wave stability. In order to more closely investigate the dependence on these parameters, we return to our most simple model, the "$i\delta$" representation. Equations 4.15-4.16 are already explicitly expressed in terms of Λ, κ_N and κ_G. We now scale each of these parameters independently by a factor, $\Lambda \rightarrow \lambda_s \Lambda$, $\kappa_N \rightarrow \lambda_N \kappa_N$ and $\kappa_G \rightarrow \lambda_G \kappa_G$. For otherwise same parameters as in Chapter IV, we vary for a specific configuration (W7-X, m=50) one of the factors λ and keep the other two constant to one. However, as the equilibrium itself is not self-consistently modified, this is strictly speaking reasonable only for small changes around $\lambda \approx 1$.

We obtain a dependence as shown in Fig. 4.8: With increasing local shear Λ, the instability clearly decreases. This gives clear evidence for our suggestion of the last chapters, that the observed ordering in stability for the various Helias configurations mainly results from differences in local shear properties. We thus have shown numerically in an actual geometry, that in ßhearlessßtellarators local shear takes over the stabilizing role, instead of global shear properties and the relating iota dependence that proved to be of essential importance in torsatrons [48].

On the specific field line of our investigation, κ_N is mostly negative in the region of mode localization, as could be seen in Fig. 4.4. A large prefactor λ_N here thus, slightly, raises instability. Geodesic curvature shows a weakly pronounced reverse dependence.

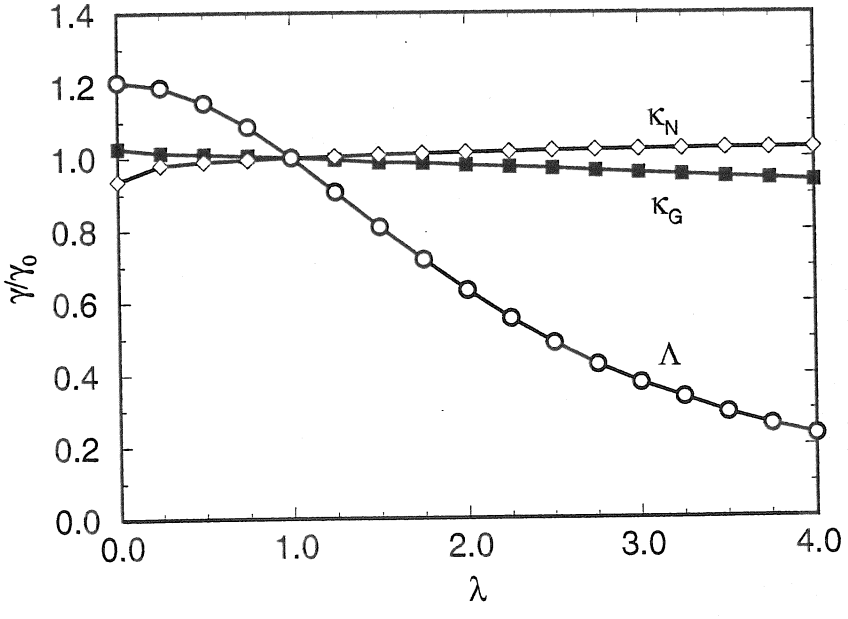

Figure 4.8. *Modification of growth rate through variation of local shear (Λ) and curvature (κ) properties by a constant factor λ.*

4.4 Radial and poloidal dependence

We drop in this section at first the constraint of a fixed field line α. The model employed here is that of trapped electron modes from section 4.2. The dependence of the frequency spectrum on this field line label α turns out to result in a highly degenerate band structure even for one mode number ($m = 50$ here) and radial label ($s = 0.25$). Real and imaginary frequencies are drawn against α in Fig. 4.9. Inset in the figure is an enlargement to show that real frequencies do not intersect but rather possess small band gaps. The whole structure could not be completely resolved numerically. It seems clear from the figure, that it turns out to be computationally very expensive if one would want to resolve the complete band structure, in two more dimensions of parameter space, for a variety of radial positions and mode numbers. For the same reasons the globally most unstable mode of a whole configuration is difficult to obtain within the framework of the ballooning mode formalism employed in this work. In the following discussion on radial features of the spectrum we thus again restrict to a local analysis on one field line ($\alpha = 0$) as before.

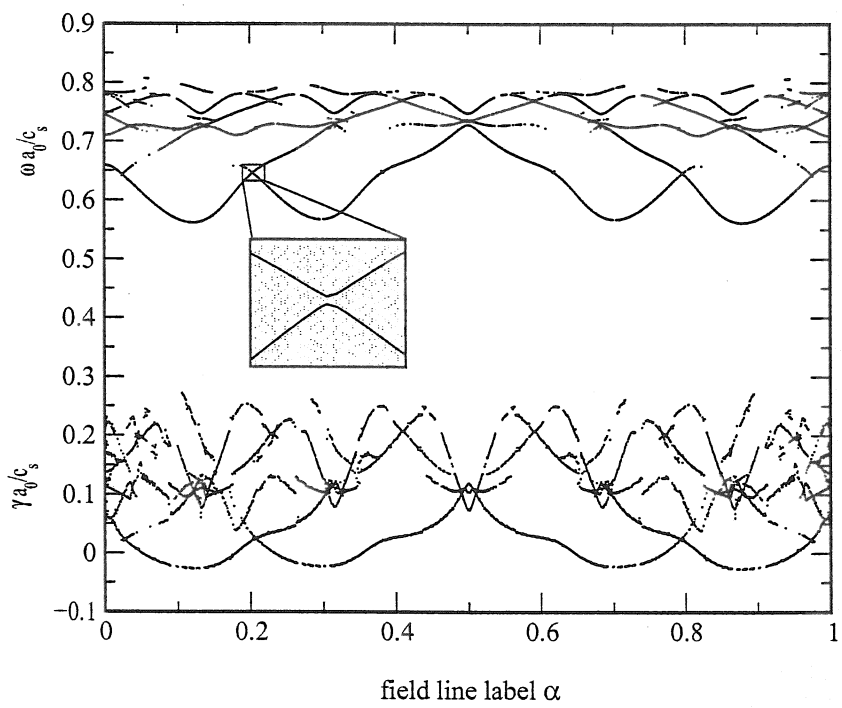

Figure 4.9. *Frequencies show a complex band structure spectrum in relation to the field line label α.*

To calculate the anomalous diffusion coefficient from linear theory can be no more than just a rough mixing length estimate. This could, however, give at least the right order of magnitude of the diffussion $D \approx \gamma \Delta_r^2$, with the radial mode width, approximated by $k_{||} = S \cdot \Delta_x \cdot k_\perp$ [42, 48], to be $\Delta_r = \rho_s/(S\Delta_\zeta)$ and the average width along

the field line

$$\Delta_\zeta^2 = \frac{\int_{-\infty}^{\infty} d\zeta |\Phi|^2 \zeta^2}{\int_{-\infty}^{\infty} d\zeta |\Phi|^2}. \tag{4.28}$$

Note that S in Δ_ζ^2 is again the local shear, in contrast to the corresponding equation in Ref. [48]. The mode width Δ_ζ along the field line and frequencies are compared radially in Fig. 4.10 for the locally most unstable $m = 50$ modes in the W7-X stellarator. Gradient parameters $L_n(s)$ and $\eta_e(s)$ are set according to experimental profiles (obtained at W7-AS) with $n/n_0 = [1 + 6.67s^{3.7}]^{-1}$ and $\hat{T}_e = [1 + 33.3s^{2.8}]^{-1}$. From mode widths and the DTEM growth rates as a function of the radial label (also Fig. 4.10) a diffusion rate of about $D \approx 0.5$ m^2/s can be inferred.

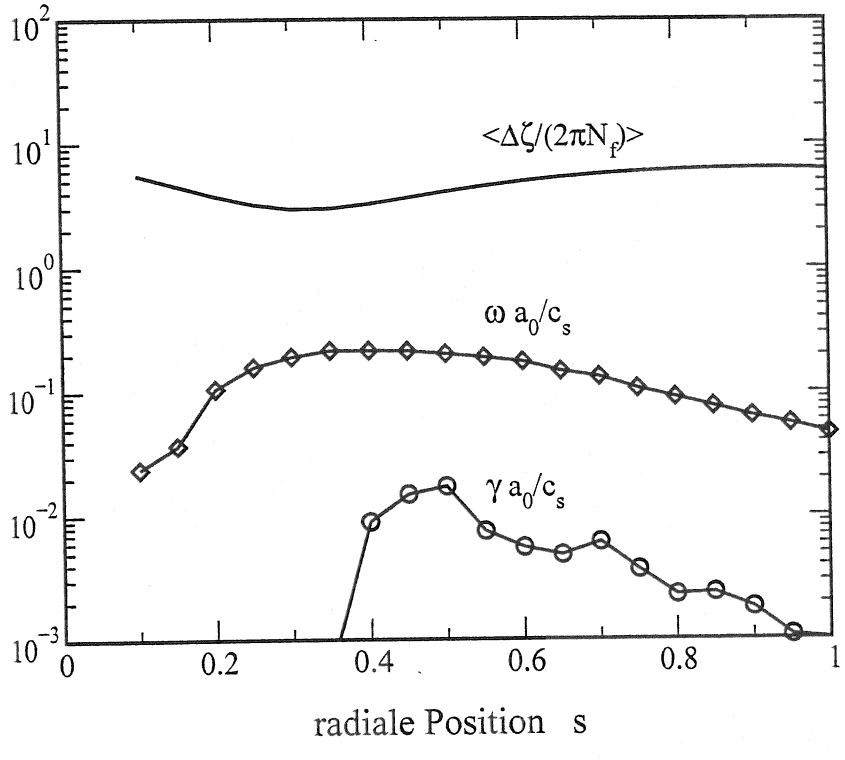

Figure 4.10. *Radial dependencies of length along the field line Δ_ζ (in units of field periods) of the locally most unstable $m = 50$ DTEM eigenfunctions in W7-X, and of linear growth rate and real eigenfrequency.*

Because of the broad radial width of exactly helical modes calculated with the above approximation for their torsatron configuration, Dominguez *et al.* concluded that in discharges with good confinement these modes should be marginally stable, and inferred only restrictions to density and temperature gradients for marginal stability. In our case, however, the most unstable modes in Helias configurations are found to be more extended along the field line than in Ref. [48]. Even more essential, the difference is due to the dominant influence of local shear in Eq. 4.27, whereas for the torsatron calculation global shear is the relevant quantity.

A direct comparison of the calculated drift wave frequencies to experimental observation may not be realized unreservedly, as linear theory can only be expected to give qualitative agreement, and a reasonable interpretation of fluctuation measurements can only be performed by nonlinear turbulence simulations. Also, a common problem in the interplay between theory and experiment is the need for non-local treatment of wave vectors in stellarator theory, while in the experiment $k_\perp$ is supplied by local values only. A typical local value of the perpendicular wave vector in experiments at W7-AS, obtained near the separatrix, has been $k_\perp = 1.74\frac{1}{cm}$ which resembles a mode number of about $m \approx 15$ in our notation. This value for m can thus be just an approximation. Still, a calculation for experimental parameters shows qualitatively sound agreement between spectral localization of maximum values, even if the highest measured fluctuation amplitude at $f \approx 3$ kHz does not exactly coincide with the largest growth rate computed for $f \approx 11$ kHz. An observed feature for a boundary value of $s \sim 0.99$ is a toroidaly highly unlocalized nature of the drift waves ($\Delta_\zeta \approx 50$). Because of the resulting relatively tight radial mode width in W7-AS (also in intermediate values of s), both DTEM and $i\delta$ model origin may here be regarded as sound possible explanations of the experimental data.

4.5 Conclusions

In this chapter we have conducted a comparative numerical study of linear drift waves in Helias type stellarator configurations. Complex frequency spectra and eigenfunctions were obtained for both an arbitrary non-adiabaticity $i\delta$ and the physically more realistic dissipative trapped electron mode. In our case of studies for a specific field line, a noticeable reduction of linear growth rates has been observed for growing stellarator optimization in HSR and W7-X compared to W7-AS. This has been understood in terms of local shear properties, which are influenced by field line torsion through increasing helicity with growing stellarator optimization. The intrinsic shearlessness of all Helias devices has the main effect on the dominant importance of local shear properties over global shear.

For the dissipative trapped electron mode we arrive at the conclusion that this regime, as far as can be judged from our local linear analysis and inferred mode widths, also remains a prospective candidate for anomalous diffusion in Helias devices. This is in contrast to [48], where the large radial width of the modes in the torsatron has led to the assumption that DTEM modes are only close to marginal stability compatible with measured transport. In Helias devices, however, the obtained solutions are associated with relatively weak localization along the field line and therefore smaller radial width (as could be seen e.g. at the inset picture in Fig. 4.5). Further, the mode width is dominated by local shear in Helias devices rather than global average shear in the torsatron.

Chapter 5

Linear gyrokinetic theory: ITG modes

The linear gyrokinetic equation is solved in the local approximation for a series of advanced stellarator configurations. Included in the model are finite ion and electron temperature gradients and finite plasma beta effects on general three-dimensional equilibria. This allows investigation of drift mode instability for core plasma parameters of a Helias fusion power plant. Numerical results for the HSR reactor configuration are presented. It is shown that consistent treatment of beta effects on the geometry is an essential ingredient for microstability calculations.

Helias stellarators are promising candidates for steady-state fusion power plants. Based on this configuration and scaled to reactor dimensions is a concept study of the stellarator power plant HSR [17]. Investigations into magnetohydrodynamic stability of HSR have shown the ability to confine a plasma up to a plasma beta beyond $\langle\beta\rangle = 4\%$ [58]. The magnetic field configuration is optimized for low neoclassical losses that are not prohibitive to ignition. In present partially optimized experiments the plasma core however is still dominated by collisional transport [3], but ion temperature gradient (ITG) driven core turbulence [4] might become significant in future devices with improved neoclassical confinement and higher core temperature.

The study in the previous chapter has been restricted to cold ions only. In a fully optimized reactor configuration, however, effects from finite ion temperature can not be neglected. The size of fluctuations itself is on the scale of several ion gyroradii and potential screening has to be taken into account. Also, a consistent treatment of finite pressure effects due to Shafranov shifting on the equilibrium is necessary. A gyrokinetic electrostatic model, that takes into account an ion temperature gradient (ITG), has been presented for stellarator geometry by Lewandowski [50, 51]. In this paper the previous work is extended to electromagnetic gyrokinetic modes. The basic equations for that mode have been formulated by Antonsen and Lane [44]. In the following, the formalism is applied to actual stellarator geometry and the effects of finite β configurations on gyrokinetic instability in a Helias reactor are investigated numerically.

5.1 The linear gyrokinetic equation

The linear electromagnetic gyrokinetic equation (GKE) describes the evolution of the nonadiabatic component h_l of the perturbed part

$$f_l = [q_l\phi(\partial_E F_{0,l}) + J_0 h_l] \tag{5.1}$$

of the distribution function for electrons and ions with charge q_l for low-frequency fluctuations obeying the drift ordering

$$\frac{h_l}{F_{0,l}} \sim \frac{e\phi}{T_l} \sim \frac{A_{||}}{B_0\rho_l} \sim \frac{\omega}{\Omega_{c,l}} \sim \frac{\rho_l}{L} \ll 1. \tag{5.2}$$

When specified, an index $l = (e, i)$ denotes the particle species. The fluctuating quantities h_l, electrostatic potential ϕ and vector potential $A_{||}$ are assumed to be small compared to their equilibrium values. The fluctuation frequency ω of interest is much lower than the gyro frequency $\Omega_{c,l} = (q_l B_0/M_l c)$, and the gyro radius $\rho_l = c\sqrt{T_l M_l}/(|q_l|B_0)$ is much smaller than a typical background scale length L of the equilibrium in a magnetized plasma with unperturbed field strength B_0. A Maxwellian

$$F_{0,l} = (\sqrt{\pi}v_{th,l})^{-3} n_0 \exp[-E/T_l] \tag{5.3}$$

with kinetic energy E is assumed for the equilibrium distribution function, so that $\partial_E F_{0,l} = -(F_{0,l}/T_l)$. Here n_0 is the unperturbed quasineutral equilibrium density and $v_{th,l} = \sqrt{2T_l/M_l}$ is the thermal velocity of the species l with mass M_l.

Following Antonsen and Lane [44], the GKE for each species is written as

$$\left(\partial_t + i\Omega_D + v_{||}\nabla_{||}\right) h = [-(\partial_E F_0)\ \partial_t + i\Omega_*]\, q\chi. \tag{5.4}$$

Here

$$\chi = J_0\phi - (v_{||}/c)J_0 A_{||} \quad \text{with} \quad J_0 = J_0(k_\perp v_\perp/\Omega_c) \tag{5.5}$$

combines the perturbed electrostatic and (parallel) electromagnetic potentials (compressional Alfvén dynamics is neglected). J_0 is a Bessel function and acts as gyroaveraging operator. The diamagnetic frequency is

$$\Omega_* = -\frac{1}{M\Omega_c}[(\mathbf{b}_0 \times \nabla F_0)\cdot \mathbf{k}_\perp], \tag{5.6}$$

and the curvature frequency is

$$\Omega_D = \frac{1}{B_0\Omega_c}[(\mathbf{B}_0 \times \nabla B)\cdot \mathbf{k}_\perp]\left(v_{||}^2 + \frac{1}{2}v_\perp^2\right). \tag{5.7}$$

In this form, the GKE is a partial differential equation that determines the temporal evolution of $h_l(\zeta, v_{||}, v_\perp)$ for each species along the coordinate ζ in the parallel direction

$\mathbf{B}_0/B_0$ of an unperturbed field line, and the perpendicular dynamics is prescribed by the wave vector $\mathbf{k}_\perp(\zeta)$. In the following, $\xi = (\zeta - q\theta)$ is used as field line label. With this an eikonal representation is employed where $\mathbf{k}_\perp = \nabla W = m\nabla\xi + \theta_k \nabla s$, with m as the (large) poloidal mode number and θ_k, the Ballooning angle, as radial mode number. In SFL coordinates, the magnetic field can be written as $\mathbf{B}_0 = \nabla\xi \times \nabla\chi_p$, where $2\pi\chi_p$ is the poloidal flux and the safety factor is $q = \partial\Psi/\partial\chi_p = 1/\iota$. The radial coordinate s is defined via the flux derivative $\Psi_s' = B_0 a_0^2$ with B_0 the field strength on axis and average minor radius a_0. The length scales representing the equilibrium (like metric elements $g^{\mu\nu} = a_0^2 \nabla x^\mu \cdot \nabla x^\nu$ and Jacobian $\hat{J}$) are normalized to this minor radius. Projecting the angle ζ onto the field line we write $a_0\nabla_{||} = J_B^{-1}\partial_\zeta$ with $J_B = \hat{B}\hat{J}$ where $\hat{B} = B/B_0$. For the assorted equations we use the following normalization scheme, where the index l refers to the appropriate species (dynamic ions for ITG, or electrons for ETG): $x = (v/v_{th,l})$, $\hat{f}_l = (f_l/F_{0,l})$, $\hat{\phi} = (|e|\phi/T_{0,l})$, $\hat{A}_{||} = A_{||}/(\beta_l B_0 \rho_{l,0})$, $\hat{t} = tc_l/L_\perp$ and $\hat{\omega} = \omega L_\perp/c_l$ with $c_l = \sqrt{T_l/M_l}$. Thus, $\hat{\chi} = J_0\hat{\phi} - x_{||}\beta J_0 \hat{A}_{||}$. For the charge, $q_l = \sigma_l|e|$ with $\sigma_i = +1$ for ions and $\sigma_e = -1$ for electrons. The species related beta is $\beta_l = 4\pi n_l T_l/B_0^2$. The gradient of the Maxwellian is written as

$$\nabla F_0 = -F_0\, L_n^{-1}\, \nabla s \left[1 + \eta_l \left(x_{||}^2 + x_\perp^2 - \frac{3}{2}\right)\right] \tag{5.8}$$

with $L_n = |\partial_s \ln n_0|^{-1}$ and $L_{Tl} = |\partial_s \ln T_l|^{-1}$ the density and temperature gradient lenghts respectively,

$$\eta_l = \frac{L_n}{L_{Tl}}, \tag{5.9}$$

and we define $L_\perp = a_0 L_n$. When the notations $\kappa_N = \hat{\nabla}\ln\hat{B}\cdot\hat{\nabla}s$ for the normal curvature, $\kappa_G = \hat{\nabla}\ln\hat{B}\cdot(\hat{\nabla}\alpha - \Lambda\hat{\nabla}s)$ for the geodesic curvature and $\Lambda = (g^{s\alpha}/g^{ss})$ are employed with $\alpha = -\iota\xi$, it can thus be written (after some transformations)

$$\sigma_l\hat{\Omega}_D = \sigma 2\frac{L_n q k_m}{\hat{B}}\left(x_{||}^2 + \frac{1}{2}x_\perp^2\right)\, g^{ss}\, \left[\left(\frac{\hat{B}}{g^{ss}}\right)^2 \kappa_N - (\Lambda + \theta_m)\, \kappa_G\right] \tag{5.10}$$

and

$$\sigma_l\hat{\Omega}_* = \sigma\hat{B}qk_m\left[1 + \eta_l\left(x_{||}^2 - x_\perp^2 - \frac{3}{2}\right)\right]. \tag{5.11}$$

Here $k_m = (m\rho_l/a_0)$ and $\theta_m = (\theta_k/m)$. Further $\Omega_{||} = \sqrt{2}\epsilon_n A_0/J_B$ with $\epsilon_n = L_\perp/R_0$ and aspect ratio $A_0 = R_0/a_0$. Declaring a new dependent variable

$$H = \hat{h} - \sigma\hat{\chi}, \tag{5.12}$$

with these definitions the GK equations are finally written as:

$$\partial_t H = -x_{||}\Omega_{||}\partial_\zeta\left(H + \sigma\hat{\chi}\right) - i\sigma\hat{\Omega}_D H - i\left(\hat{\Omega}_D + \hat{\Omega}_*\right)\chi. \tag{5.13}$$

5.2 The gyrokinetic Poisson equation

The electrostatic potential is connected to the distribution function via the Poisson equation

$$\nabla_\perp^2 \phi = -4\pi|e|(n_i - n_e) = -4\pi|e|\left[\int d^3v f_i - \int d^3v f_e\right]. \tag{5.14}$$

with

$$f_e = q_e\phi\ \partial_E F_{0e} + \delta_e J_0 h_e = +(|e|\phi/T_e)F_{0e} + \delta_e J_0 h_e \tag{5.15}$$

and

$$f_i = q_i\phi\ \partial_E F_{0i} + \delta_i J_0 h_i = -(|e|\phi/T_i)F_{0i} + \delta_i J_0 h_i. \tag{5.16}$$

We introduce δ_l as an artificial parameter that is unity in the general case where both species are evolved, and is set to ($\delta_i = 1$, $\delta_e = 0$) for ITG modes with adiabatic electrons or vice versa to ($\delta_i = 0$, $\delta_e = 1$) when ETG modes with adiabatic ions are considered.

The Debye term in the Poisson equation is kept for ETG modes only, as the electron gyro radius ρ_e may be in the same order as the Debye length $\lambda_D = \sqrt{T_{l0}/4\pi n_0 e^2}$. The temperature ratio here is defined as $\tau = (T_{0i}/T_{0e})$. Then one has with $\hat{\phi} = (|e|\phi/T_e)$:

$$\begin{aligned} -k_\perp^2\phi = -4\pi|e|\Big[&\delta_e \int d^3v J_0 \hat{h}_i F_{oi} - \hat{\phi}\int d^3v F_{oi} \\ &-\delta_i \int d^3v J_0 \hat{h}_e F_{oe} - \tau\hat{\phi}\int d^3v F_{oe}\Big]. \end{aligned} \tag{5.17}$$

The Maxwellian integrals can be explicitly evaluated with $\int d^3v = 2\pi \int dv_\perp dv_{||} v_\perp$. In the same normalization as before one thus gets

$$\begin{aligned} |\hat{\nabla}W|^2\hat{\phi} = \frac{(a_0/\lambda_D)^2}{\sqrt{2\pi}}\Big[&-\hat{\phi}(\tau+1)\frac{\sqrt{\pi}}{2} + \delta_i \int dw_\perp dw_{||} w_\perp J_0 \hat{h}_i\ e^{-w_\perp^2 - w_{||}^2} \\ &-\delta_e \int dz_\perp dz_{||} z_\perp J_0 \hat{h}_e\ e^{-z_\perp^2 - z_{||}^2}\Big]. \end{aligned} \tag{5.18}$$

Here x is substituted by w for ions and by z for electrons. When $\hat{h} = H + \sigma\hat{\chi}$ is re-expressed in the dependent variables, the remaining integral can be partially evaluated in terms of the modified Bessel function I_0:

$$\int dx_\perp dx_{||} x_\perp J_0^2(\rho_l k_\perp x_\perp)\exp[-x_\perp^2 - x_{||}^2] = (\sqrt{\pi}/2)I_0(y)\exp[-y] \tag{5.19}$$

where $y = (\rho_{th,l}k_\perp)^2/2 = (\rho_l k_\perp)^2 = k_m^2|\hat{\nabla}\xi + \theta_m\hat{\nabla}s|^2$. Further we use that $\int_{-\infty}^{+\infty} dx_{||} x_{||}\exp[-x_{||}^2] = 0$, and $D \equiv \sqrt{2\pi}(\lambda_D/a_0)^2|\hat{\nabla}W|^2 = 2\sqrt{2\pi}y(\lambda_D/\rho_l)^2$ is abbreviated. Thus one can write in a compact form:

$$\begin{aligned} \hat{\phi} = &\frac{\delta_i}{G}\int dw_\perp dw_{||} w_\perp J_0(\sqrt{2y_i}w_\perp) H(\zeta, w_\perp, w_{||})\exp\left[-w_\perp^2 - w_{||}^2\right] \\ &-\frac{\delta_e}{G}\int dz_\perp dz_{||} z_\perp J_0(\sqrt{2y_e}z_\perp) H(\zeta, z_\perp, z_{||})\exp\left[-z_\perp^2 - z_{||}^2\right] \end{aligned} \tag{5.20}$$

with $G = (\sqrt{\pi}/2)\,[1 + \tau - \delta_i I_0(y_i)\exp(-y_i) - \delta_e I_0(y_e)\exp(-y_e)] - D$. For ITG modes ($\delta_i = 1$) the Debye term D is neglected because $(\lambda_D/\rho_i) \ll 1$. G thus reduces to $G = (\sqrt{\pi}/2)[1 - \delta_e + \tau - I_0(y_i)\exp(-y_i)]$ because $y_e = y_i/\mu_M \ll 1$ with $\mu_M = M_i/M_e$. In this case, one is usually not interested in the high-frequency electron oscillations, and the GKE for the electrons may be computed with fixed electromagnetic potentials that are evaluated on the ion time scale only [59].

In the following numerical examples only electrostatic ITG modes with adiabatic electrons ($\delta_e = 0$) will be considered. A possible future extension of such an ITG model with adiabatic electrons is to combine our electromagnetic approach with the electrostatic hybrid kinetic ion / fluid electron model by Lewandowski [51], or with a nonadiabatic trapped electron response [60].

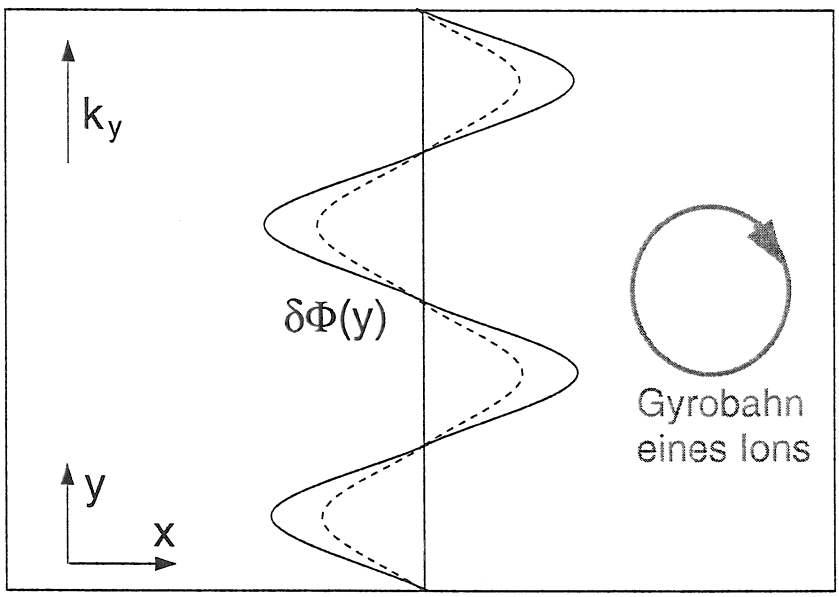

Figure 5.1. Due to their gyro motion the ions feel an average electric field (dotted line), which is less than the real field at the gyro center (dark line).

5.3 Gyrokinetic Ampere's law

The parallel vector potential component $A_{||}$ is evaluated via Ampere's law $\nabla \times \tilde{\mathbf{B}} = (4\pi/c)\tilde{\mathbf{j}}$, or for shear-Alfvén contributions only:

$$(\nabla \times \tilde{\mathbf{B}})_{||} = \nabla_\perp^2 A_{||} = -\frac{4\pi}{c}\int d^3v v_{||}|e|(f_i - f_e). \tag{5.21}$$

Herein the adiabatic contributions of f vanish, because in the parallel velocity integral again negative and positive parts cancel. After evaluation of some of the integrals like before, one again arrives in the above normalization at a compact explicit form for the

vector potential:

$$\hat{A}_{||} = \frac{\delta_i}{C}\int dw_\perp dw_{||} w_\perp w_{||} J_0(\zeta, w_\perp) H(\zeta, w_\perp, w_{||}) \exp[-w_\perp^2 - w_{||}^2] - \frac{\delta_e}{C}\int dz_\perp dz_{||} z_\perp z_{||} J_0(\zeta, z_\perp) H(\zeta, z_\perp, z_{||}) \exp[-z_\perp^2 - z_{||}^2] \tag{5.22}$$

with $C = (\sqrt{\pi}/2)\left[\frac{1}{2}\sqrt{2}(\delta_i y_i + \delta_e y_e) - \frac{1}{2}\beta(\delta_i I_0(y_i)\exp(-y_i) + \delta_e I_0(y_e)\exp(-y_e))\right]$.

5.4 Set of equations for explicit numerical evaluation

The compound distribution function $H_{R,I}$, the electrostatic potential $\hat{\phi}_{R,I}$ and vector potential $\hat{A}_{||\,R,I}$, and thus also $\hat{\chi}_{R,I}$, are all complex quantities. With $G(\zeta)$, $C(\zeta)$, $\hat{\Omega}_{||}(\zeta)$, $\hat{\Omega}_D(\zeta, x_\perp, x_{||})$ and $\hat{\Omega}_*(\zeta, x_\perp, x_{||})$ as defined above one thus arrive at the following set of eight equations:

$$\partial_t H_{Rl} = -x_{||}\Omega_{||}\partial_\zeta\left(H_{Rl} + \sigma_l \hat{\chi}_{Rl}\right) + \sigma_l \hat{\Omega}_D H_{Il} + \left(\hat{\Omega}_D + \hat{\Omega}_*\right)\hat{\chi}_{Il} \tag{5.23}$$

$$\partial_t H_{Il} = -x_{||}\Omega_{||}\partial_\zeta\left(H_{Il} + \sigma_l \hat{\chi}_{Il}\right) - \sigma_l \hat{\Omega}_D H_{Rl} - \left(\hat{\Omega}_D + \hat{\Omega}_*\right)\hat{\chi}_{Rl} \tag{5.24}$$

$$\hat{\phi}_{R,I} = (1/G)\sum_l \delta_l \sigma_l \int dx_\perp dx_{||} x_\perp J_0 H_{R,I} \exp\left[-x_\perp^2 - x_{||}^2\right] \tag{5.25}$$

$$\hat{A}_{||\,R,I} = (1/C)\sum_l \delta_l \sigma_l \int dx_\perp dx_{||} x_\perp x_{||} J_0 H_{R,I} \exp[-x_\perp^2 - x_{||}^2] \tag{5.26}$$

For numerical solution of the GKE an explicit two-step Lax-Wendroff-Richtmyer scheme is used [61]. In this initial-value approach, the most unstable eigenmode settles after a transient initial phase that is dependent on the width Δ of the initial Gaussian perturbation

$$\chi(t=0) = \exp[-\zeta^2/\Delta^2]. \tag{5.27}$$

The instantanous real eigenfrequency ω_R and growth rate γ are obtained via the relations

$$\gamma = \partial_t \ln\sqrt{\bar{\phi}_R^2 + \bar{\phi}_I^2} \tag{5.28}$$

and

$$\omega_R = [(\bar{\phi}_I/\bar{\phi}_R)/(1 + (\bar{\phi}_I/\bar{\phi}_R)^2] \cdot [\partial_t \ln\bar{\phi}_R - \partial_t \ln\bar{\phi}_I] \tag{5.29}$$

evaluated for an average

$$|\bar{\phi}| = \frac{1}{2\zeta_\infty}\int_{\zeta_m-\zeta_\infty}^{\zeta_m+\zeta_\infty} \hat{\phi}(\zeta')\mathrm{d}\zeta'. \tag{5.30}$$

over the relevant parallel computational domain [59] after each complete time step. More details on explicit and semi-implicit numerical procedures for solving the linear GKE can e.g. be found in references [51] and [59].

5.5 Simple tokamak model: $\hat{s} - \alpha_M$ geometry

For the axisymmetric magnetic field configuration of a tokamak with large aspect ratio $A_0 = R_0/a_0$, a simple representation of the field geometry is frequently used. It takes into account the global magnetic shear $\hat{s} = (a_0/q)(\partial q/\partial r)$ and Shafranov shift $\alpha_M = -q^2 R(\partial\beta/\partial r)$ for circular flux surfaces. The magnetic field strength is then $\hat{B} = 1 + (1/A_0)\cos\theta \approx 1$ with $b = 1$. The relevant metric elements are $g^{ss} = 1$ and $g^{\alpha\alpha} = (b\hat{B})^2/g^{ss} + \Lambda^2 g^{ss} = 1 + \Lambda^2$ with $\Lambda = g^{s\alpha}/g^{ss} = \hat{s}\theta - \alpha_M \sin\theta$. The curvature terms are $\kappa_N = -(1/A_0)\cos\theta$ and $\kappa_G = (1/A_0)\sin\theta$. The Jacobian is $J_B = 1$ and thus $(1/J_B)\partial_\zeta = (1/q)\partial_\theta$ when, as ususal in tokamak literature, the coordinate θ is used as a label along the field line instead of ζ. It is also common for tokamaks to define as field line label $\xi = \zeta - q\theta$ instead of $\alpha = \theta - \iota\zeta$, so that

$$k_\perp = m|\nabla\xi| = mq|\nabla\alpha| = mq\sqrt{1 + (\hat{s} - \alpha_M \sin\theta)^2}. \tag{5.31}$$

The curvature frequency now is

$$\hat{\Omega}_D = -2k_m\epsilon_n \left(x_{||}^2 + (1/2)x_\perp^2\right)\left[\cos\theta + (\hat{s}\theta - \alpha_M \sin\theta)\sin\theta\right]. \tag{5.32}$$

These definitions describe the standard case for tokamak geometry and allow for a benchmark with existing codes and with numerically tabulated circular tokamak equilibria (e.g. of Tore Supra). A $\rho_i k_\theta$ spectrum obtained with our code for the standard Cyclone base case data set [4] in figure 5.2 shows good agreement to other gyrokinetic codes (compare to figure 1 in Dimits *et al* [4]).

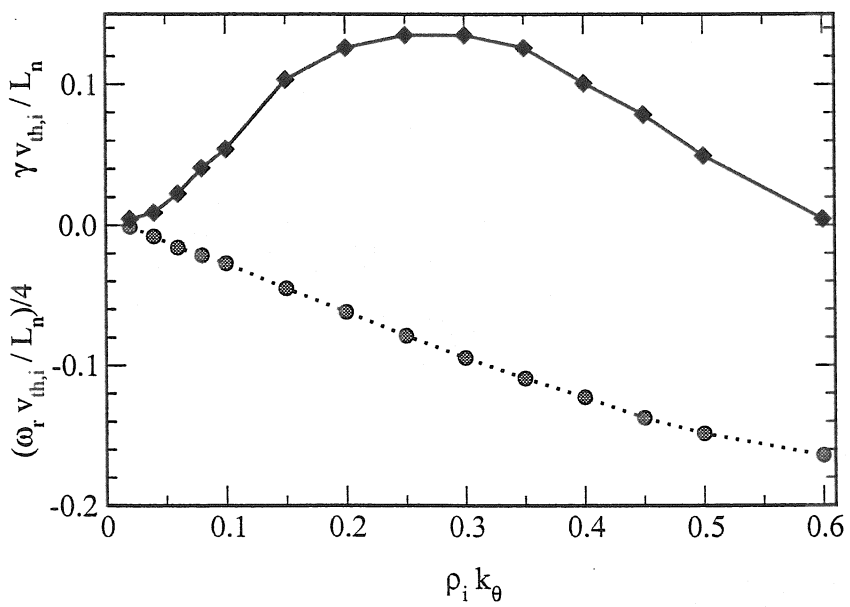

Figure 5.2. *$\rho_i k_\theta$ benchmark spectrum of electrostatic ITG growth rate and real frequency for standard Cyclone base case data in circular tokamak geometry [4].*

5.6 HSR finite beta equilibrium

The metric quantities in a stellarator vary rapidly along a field line due to helical modulations in contrast to tokamak geometry. In figure 5.3 the perpendicular wave vector $|\rho_i k_y| = |\rho_i k_\perp / k_m| = \sqrt{g^{\xi\xi}}$ is shown for two different cases of Helias stellarator equilibria. In ballooning space $g^{\xi\xi}$ is a secular quantity increasing proportional to shear with the parallel coordinate $(\zeta - \zeta_0)$, in relation to a location point (θ_0, ζ_0) on the flux surface. Global shear is very low in advanced stellarators, but high local shear leads to strong variations of the wave vector.

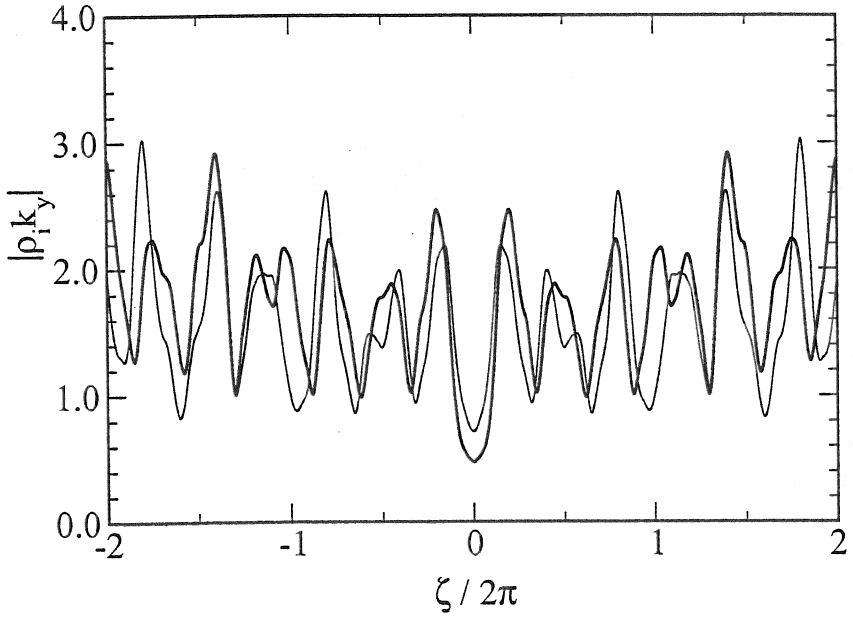

Figure 5.3. *Perpendicular wave vector $|\rho_i k_y| = |\rho_i k_\perp / k_m|$ along a field line for a vacuum Helias configuration HSR-B0 (thin line) and for 5% beta HSR-B5 (bold line).*

The Helias reactor HSR is optimized for reduction of the currents flowing in the plasma to a low level. The currents parallel to the magnetic field (Pfirsch-Schlüter currents) are smaller than the diamagnetic currents [17]. This results in a low Shafranov shift for increasing beta. The rotational transform decreases with rising plasma pressure and an $\iota = 5/6$ resonance appears around $\langle\beta\rangle = 4.2\%$. It has been demonstrated that below this margin the HSR Helias reactor configuration shows stability with respect to local ballooning modes, Mercier and resistive interchange criteria and to global ideal MHD modes [58]. Still, the deformation of the plasma column through Shafranov shift has effects on the equilibrium and geometric properties that may not be neglected in microstability simulations. In this section the gyrokinetic stability of a series of six HSR equilibria for plasma beta values between $\langle\beta\rangle = 0$ and $\langle\beta\rangle = 5\%$ is investigated. The same numerical equilibria are used as obtained by E. Strumberger in Ref. [58]. In the following we term the single equilibria as "HSR-B0" for the vacuum case, "HSR-B1" for

the $\langle\beta\rangle = 1\%$ case and so on. The poloidal cross sections of two stellarator-symmetry planes (termed "triangular" and "bean-shaped" in the following) for the two extremal configurations of zero and maximum beta are shown in Fig. 5.4. We define the location point (θ_0, ζ_0), that has to be specified in ballooning space, as on the outboard midplane of the bean shaped cross section, and $(\theta_0, \zeta_1) = (\theta_0, \zeta_0 + \pi/N_f)$ on the outboard midplane of the triangular cross section.

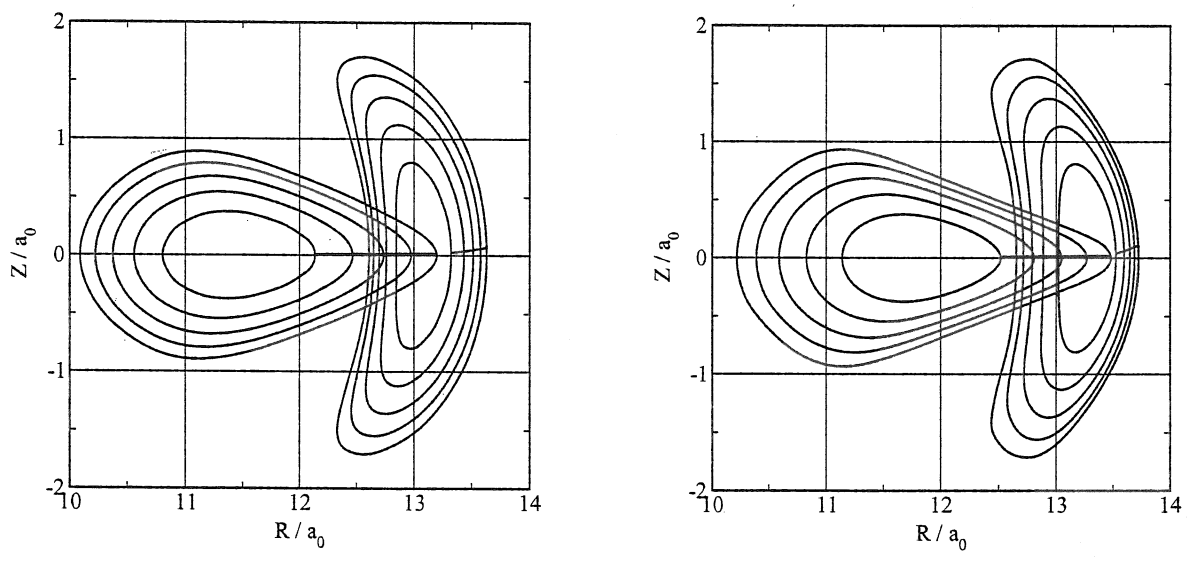

Figure 5.4. *Plasma cross section on the two Helias stellarator reactor symmetry planes of HSR-B0 for $\langle\beta\rangle = 0$ (left) and shifted due to finite plasma pressure for $\langle\beta\rangle = 5\%$ (right) of HSR-B5.*

5.7 Finite beta equilibrium effects on ion temperature gradient instability

The effect of finite plasma pressure Helias reactor equilibria on microinstability is demonstrated in this section with numerical examples for electrostatic ITG modes with adiabatic electrons. Electromagnetic ITG simulations including nonadiabatic electron dynamics with the further complication of destabilization of the kinetic ballooning mode branch (KBM), as well as a discussion of ETG modes in stellarator geometry will be left for future work. Thus, in the following we set $\delta_i = 1$, $\delta_e = 0$ and the parameter $\beta = 0$ in the GKE. It shall be assumed that the profiles $(T(s)/T_0)$ and $(n(s)/n_0)$ change self-similarly with increasing plasma pressure and consequently the profile scales ϵ_n and η_i remain unchanged during variation of the finite $\langle\beta\rangle$ equilibrium. If not explicitly specified otherwise in the following, the parameters in the GKE are set to $\epsilon_n = 0.15$, $\eta_i = 6.5$, $\tau = 1$ and $k_m = 0.8$.

The standard normalization of frequencies is to $(c_i/L_\perp)$. For the dependence of c_i on the plasma pressure it may be assumed that $T_i(\beta) \sim \sqrt{\beta}$. For a scan in finite beta equilibria, however, one might want to chose physical units instead, or a normalizati-

on to a fixed reference temperature, as the normalization should not depend on the quantity whose variation is considered. For a reference thermal speed c_0 we here chose $T(\beta = 0.05)$ such that $\bar{\omega} = \hat{\omega}(\beta/0.05)^{1/4}$ when compared to the frequency $\hat{\omega}$ calculated in the standard normalization.

A strongly stabilizing effect of finite plasma pressure entering into ITG mode analysis via the Shafranov shift of the equilibrium is well known from the investigation of shaped $(s - \alpha)$ tokamak models (see e.g. reference [62]). In that case, axisymmetric shaping effects of elongation, triangularity and Shafranov shift can be described by single variable parameters when determining the metric quantities. For a stellarator such simple models can not be obtained. We therefore have to make use of precalculated, self-consistently iterated tabular representations of finite beta equilibria as described in the previous section.

For the present HSR configuration it has been found that the finite plasma pressure leads to an increase of the magnetic well from $V'' = -0.68\%$ in the vacuum case to $V'' = -9.14\%$ for $\langle\beta\rangle = 5\%$ [58]. This enters into the GKE description of ITG modes through the curvature drift term $\hat{\Omega}_D$, where both normal and geodesic curvature, and local shear are modified by the transition of the equilibrium to higher beta. From a basic dispersion relation analysis in the fluid electrostatic limit of ITG description [63] it becomes clear that for $\hat{\Omega}_D < 0$ the frequency becomes imaginary and the mode is destabilized. In figure 5.5 the variation of $\hat{\Omega}_D(\zeta)$ along a field line is shown for the vacuum and high beta cases HSR-B0 and HSR-B5. The destabilizing region in ballooning space has significantly shrunk for large plasma pressure.

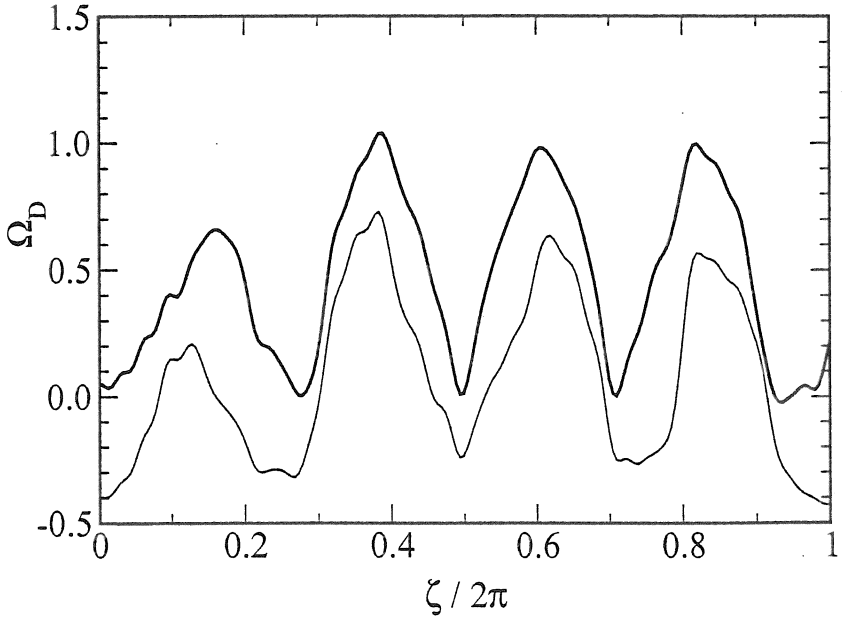

Figure 5.5. *Curvature drift frequency $\hat{\Omega}_D(\zeta)$ for $k_m = 1$ in ballooning space along the field line for HSR-B0 (thin line) and for HSR-B5 (bold line).*

For each of these two configurations mode number spectra of the growth rate $\hat{\gamma}$ are calculated as a function of $k_m = \rho_i k_\theta$. In the standard normalization, as shown in the figure, the maximum growth rate clearly decreases for the high beta case by around one third compared to the vacuum configuration. This is what could already have been expected by the qualitative change of the curvature frequency $\hat{\Omega}_D$ as seen in figure 5.5.

Nevertheless, normalized by a reference thermal speed c_0, the growth rate $\bar{\gamma}$ is increased again by the corresponding factor $(5^{1/4})$ when pressure quintuples. Considering the maximum growth rate thus nothing is gained, and stabilizing and destabilizing effects approximately even out.

The finite pressure shaping of the geometry, however, also shifts the maximum in the growth rate to higher values of the perpendicular wave vector. A similar shift has been observed also for tokamaks with increasing ellipticity [64]. There it has been argued that the smaller wavelength of potential perturbations in a mixing lengths picture directly results in a reduction of transport by shortening the correlation length of fluctuations.

Note that in our case the finite pressure flux surface shaping is accompanied by an according increase of ρ_i that enters into the normalized $\rho_i k_\theta$ in such a way that, again, suppression of the resulting turbulence is ineffective.

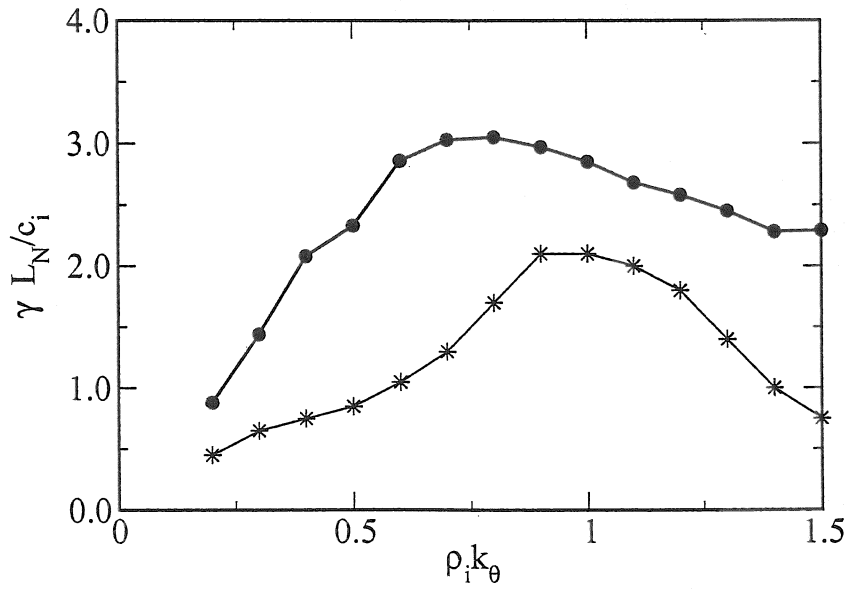

Figure 5.6. *Perpendicular mode number spectra of the growth rate $\hat{\gamma}$ for the cases HSR-B0 (bold line, circles) and HSR-B5 (thin line, stars). A reduction of the destabilizing region as seen in figure 5.5 with rising beta results in a decrease of the maximum growth rate. The shift of the spectrum to shorter wavelengths is a further effect of plasma shaping. Note that here the normalization also depends on beta.*

These results are illustrated in figure 5.7, where k_m has been varied for each equilibrium to find the maximum growth rate: The lowering of $\hat{\gamma}$ with rising plasma pressure by the Shafranov shift in standard normalization (bold solid line) is compensated when a normalization to a reference temperature is applied (thin solid line). For a tokamak model, where a continous variation of beta is possible, it has been reported by Rewoldt *et al.* that a maximum in the growth rate can be observed (there for different parameters and inclusion of trapped electrons at $\beta \approx 0.5\%$) [62]. For HSR the perpendicular wave number of the most unstable solution for each configuration (dashed line) gradually increases with rising beta, when normalized to the equally increasing beta-dependent gyro radius. This shows the important effect of flux surface shaping on microinstabilities in a stellarator, but as the shaping in our case is due to rising pressure, no consequent suppression of transport can be expected.

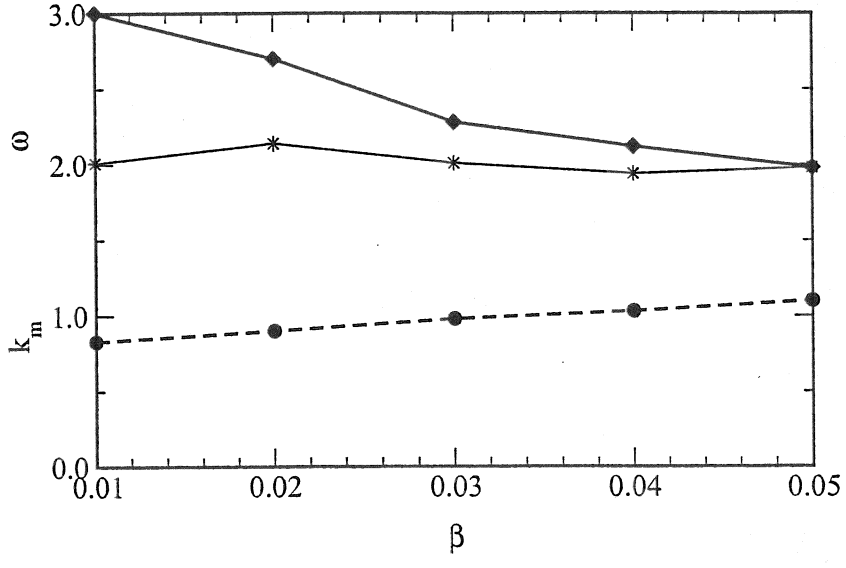

Figure 5.7. *Effect of gradually rising β in a Helias reactor configuration HSR: In a standard normalization, that depends on beta itself, a beta stabilization is observed (bold line). In a normalization to a reference temperature ($c_0 = c_{i,5\%}$) the linear growth rate (thin line) remains on a similar level throughout. Dotted line: The perpendicular wave vector $\rho_i k_\theta$ in units of the (varying) gyro radius increases with rising pressure.*

5.8 Parameter dependence of ITG growth rates

Next, some of the free parameters appearing in the GKE are varied. It has been assumed in the previous calculations that the radial mode number, specified by the ballooning angle θ_k, is zero. In figure 5.8 this parameter is varied for HSR-B3 at $\beta = 0.03$, $k_m = 0.8$ and the other settings as above. The largest growth rate indeed appears for $\theta_k = 0$. This characteristic may be responsible for the radially elonged streamer formation that

is observed in nonlinear ETG turbulence studies [65]. For ITG modes these streamers are broken up by secondary nonlinear processes and poloidal shear flows. Figure 5.9 shows how the growth rate increases with the relative ITG scale η_i.

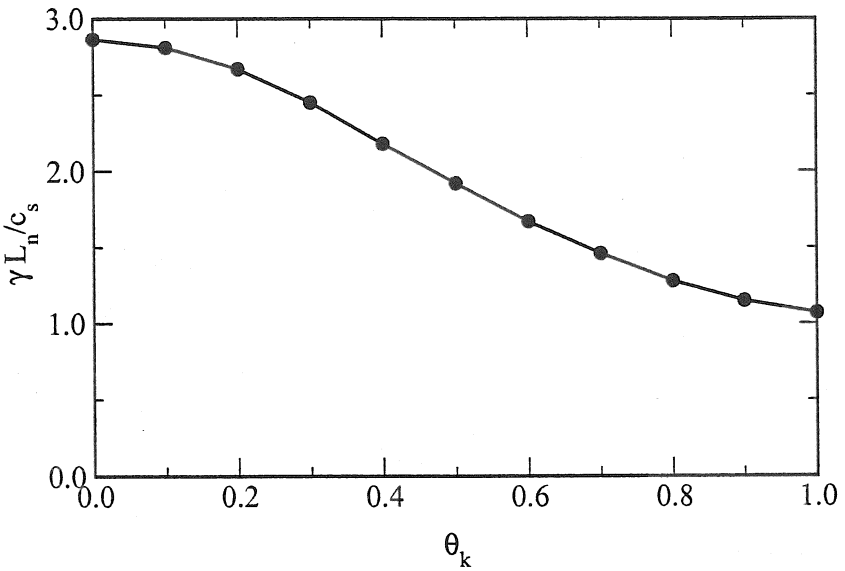

Figure 5.8. *Variation of the radial mode number ballooning parameter θ_k for HSR-B3. The maximum growth rate occurs for $\theta_k = 0$.*

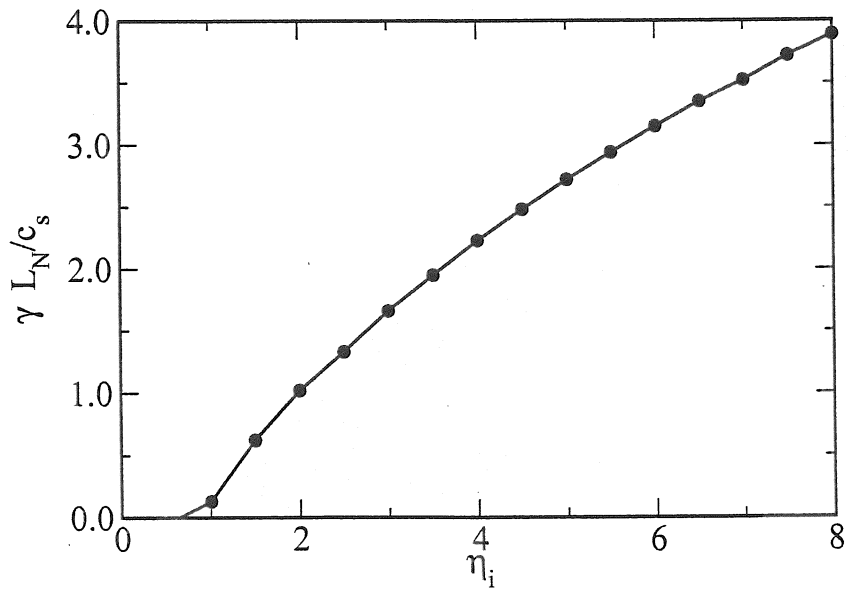

Figure 5.9. *Increase of linear growth rate $\hat{\gamma}$ with variation of $\eta_i = L_n/L_{Ti}$*

5.9 Negative shear in tokamaks and Helias stellarators

The toroidal ITG mode in a tokamak is known to be effectively stabilized by negative shear $\hat{s} < 0$ [66]. By considering equations (8-10) it can be noted that the sign of shear enters via Λ only into the curvature drift frequency $\hat{\Omega}_D$, when the Bloch number θ_k is zero. For $\theta_k = 0$ the other contributions into the Bessel functions and scaling factors G and C of the electromagnetic potentials only appear via Λ^2. As a consequence the width of the region of destabilizing negative $\hat{\Omega}_D$ in ballooning space is modified by a change of sign in Λ according to the combination of κ_N and κ_G. The situation is illustrated in figure 5.10: For a circular tokamak with shift $\alpha_M = 0$ as described by equation (25) the value of $\hat{\Omega}_D$ for positive global shear $\hat{s} = 0.8$ is shown by the bold curve. For negative shear $\hat{s} = -0.8$ the unstable region around the localization point ($\zeta_0 = 0$) is reduced significantly (dashed line).

An interesting question is whether the overall negative global shear of a Helias stellarator contributes to a favourable stabilization of the ITG mode. The flux surface average at half minor radius for HSR is about $\hat{s} = -0.1$. A much larger contribution results however from local modifications to the shear, and the well of $\hat{\Omega}_D$ acquires a more complicated structure, as it is illustrated in figure 5.10 by the thin curve. The helical modulations dominate the effect of toroidicity and also lead to a more detailed structure of the eigenmodes themselve. In chapter 6 we will see the significance of the local structure of shear for the case of drift-Alfvén wave turbulence, where local shear acts as an efficient stabilizing agent in low-global-shear Helias stellarators [10].

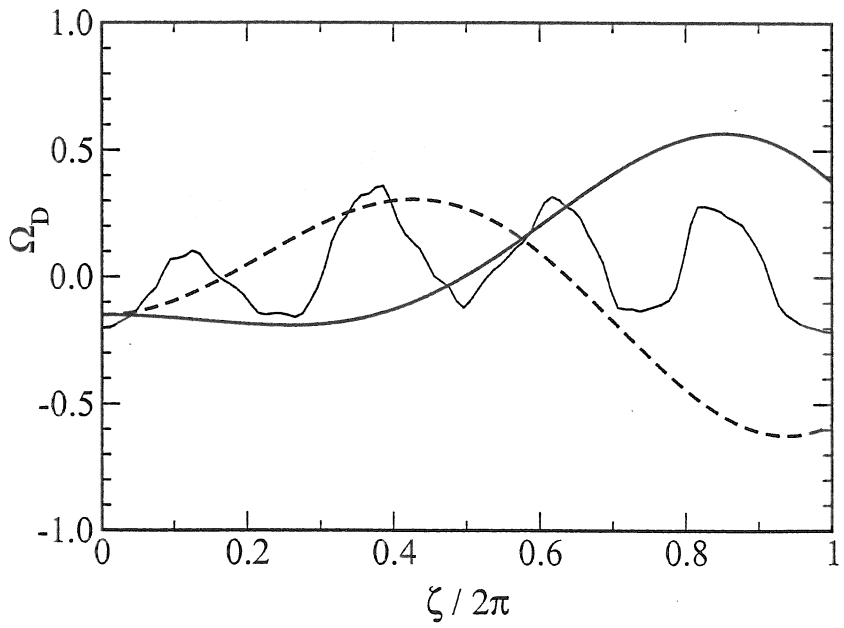

Figure 5.10. *Curvature drift frequency $\hat{\Omega}_D$ in ballooning space for the cases of a circular tokamak with global shear $\hat{s} = 0.8$ (bold curve), $\hat{s} = -0.8$ (slashed curve) and HSR-B0 (thin curve) with strong helical variations of local shear.*

5.10 Conclusions

The gyrokinetic equation has been solved numerically for a series of finite beta Helias stellarator reactor configurations, and growth rates for the ITG mode have been obtained. The Shafranov shifting of rising plasma pressure on the equilibrium is shown to have a stabilizing effect by reducing the regions of negative curvature drift frequency in ballooning space. Subtracting out the further effects of rising beta on the standard normalization, it is found that the overall change of maximum linear growth rate and corresponding wave length in physical units is negligible. Finite beta stabilization of ion temperature gradient modes therefore is present in Helias reactor configurations but has no direct observable effect on suppression of transport.

Our present ITG microinstability studies do not yet include effects of trapped electrons, which can be expected to be of importance, and are radially local. Global mode calculations in Helias geometry are currently being prepared by R. Kleiber for linear resistive drift-ballooning modes [52] and by R. Hatzky for ITG modes [67].

Chapter 6

Drift-Alfvén wave turbulence

Direct numerical simulations of drift-Alfvén wave turbulence in actual three-dimensional stellarator geometry are reported. It is found that the local metric has significant influence on instability and transport and that local shear contributes as the principal damping mechanism in low-global-shear field configurations. The transition from simple tokamak to stellarator geometry and effects on plasma edge turbulence and anomalous transport are investigated in flux-tube models of the equilibria and suitable interpolations.

In stellarator experiments the plasma edge region is found to be dominated by turbulent diffusion that shows similar transport properties like in tokamak devices [68]. Measured frequency spectra of plasma edge fluctuations are similar and were argued to display universality in behaviour [69]. This comes to reason, as the basic mechanisms of drift wave instability are fundamentally the same in tokamaks and stellarators alike and independent from geometry. Gradients of density, electron and, sufficiently steep, of ion temperature provide a source of free energy that may be tapped by dissipative processes and Alfvén wave dynamics [36]. Damping effects, on the other hand, are due to magnetic and velocity shear [70] and may differ for specific geometries.

The previous chapters as well as recent results in nonlinear simulations of drift waves in shaped tokamak equlibria [72] show considerable influence of magnetic field geometry on instability and transport. Field line shaping in a tokamak is usually due to secondary properties like e.g. elongation of the plasma torus in vertical direction. Stellarators on the other hand generically show a non-trivial geometry from the first [71].

In this chapter we present the first direct numerical simulation of plasma turbulence in actual stellarator geometries and show that the local metric indeed determines instability and transport. This carries significant consequences: Our results suggest that inclusion of the exact metric for drift-Alfvén simulations is an important ingredient. Also in tokamak research care has to be taken especially when local shear is large near an X-point of the separatrix. For advanced stellarators, turbulent transport may be reduced by proper optimization of the magnetic field geometry and further enhance the reactor prospects of these configurations.

6.1 Direct numerical simulation of drift-Alfvén wave turbulence

For our studies on geometry dependence of turbulence we use a cold ion model for low frequency plasma edge turbulence with electromagnetic, isothermal electron dynamics [37], which represents the most basic model containing the principal interactions of drift wave physics: free energy liberated from the background gradient is transferred from pressure fluctuations to ExB eddies by coupling of both to parallel currents. Fluid equations are used for both species. We apply drift ordering and retain advection by the $E \times B$ velocity and the contributions to the parallel gradient due to the perturbed magnetic field as the only nonlinearities. The electric field is given by

$$\mathbf{E} = -\nabla\phi - (1/c)\partial_t A_{||}\mathbf{b}, \tag{6.1}$$

where ϕ and $\mathbf{A}$ are the electrostatic and vector potential, respectively. The unit vector $\mathbf{b}$ is parallel to the equilibrium magnetic field $\mathbf{B}$, and we abbreviate $\partial/\partial t \equiv \partial_t$. The dynamics is described by a conservation law for the total current $\mathbf{J}$, a parallel equation of motion for electrons, and a continuity equation for electron density n_e. The parallel velocity $u_{||}$ of the ions results from $E_{||}$, and their perpendicular velocity

$$\mathbf{u}_\perp = \mathbf{v}_E + \mathbf{u}_p \tag{6.2}$$

is the same $\mathbf{v}_E = (c/B^2)\mathbf{E}\times\mathbf{B}$ as for electrons with an additional $\mathbf{u}_p = -(M_i c^2/eB^2)(\partial_t + \mathbf{v}_E\cdot\nabla)\nabla_\perp\phi$ correction due to finite inertia. The nonlinear advective derivative is written as $D_t = \partial_t + \mathbf{v}_E \cdot \nabla$, and the nonlinear parallel gradient is

$$\nabla_{||} = \mathbf{b}\cdot\nabla - \hat{\beta}(\mathbf{b}\times\nabla A_{||})\cdot\nabla. \tag{6.3}$$

We define the ion sound speed $c_s = \sqrt{T_e/M_i}$, perpendicular scale lenghth $L_\perp$ and drift scale $\rho_s = \sqrt{T_e M_i}c/eB$, and normalize ϕ to T_e/e, n to n_e, $u_{||}$ to $c_s(qR/L_\perp)$, $J_{||}$ to $n_e e c_s(qR/L_\perp)$, A to $B\rho_s\hat{\beta}(qR/L_\perp)$ and Ω to $\rho_s^{-2}T_e/e$. $\nabla_\perp$ appears as $\rho_s\nabla_\perp$, $\nabla_{||}$ as $qR\nabla_{||}$ and ∂_t as $(L_\perp/c_s)\partial_t$. Terms small by factors of order the parallel/perpendicular wavenumber ratio, $k_{||}/k_\perp$, are dropped. In this normalization the system of equations is

$$\begin{aligned}
D_t\Omega &= \nabla_{||}J_{||} - \mathcal{K}(n), && (6.4)\\
\hat{\mu}D_t J_{||} &= -\hat{\beta}\partial_t A_{||} + \nabla_{||}(n-\phi) - \omega_n\hat{\beta}\partial_y A_{||} - \hat{\mu}\nu J_{||}, && (6.5)\\
D_t n &= -\omega_n\partial_y\phi + \nabla_{||}(J_{||} - u_{||}) - \mathcal{K}(n-\phi), && (6.6)\\
\epsilon D_t u_{||} &= -\nabla_{||}n + \omega_n\hat{\beta}\partial_y A_{||}. && (6.7)
\end{aligned}$$

with two auxiliary relations

$$\Omega = \rho_s^2\nabla_\perp^2\phi \tag{6.8}$$

and

$$J_{||} = -\nabla_\perp^2 A_{||}. \tag{6.9}$$

The curvature operator

$$\mathcal{K} = -L_\perp(\mathbf{b} \times \nabla \log B^2) \cdot \rho_s \nabla \tag{6.10}$$

is scaled by T/e and normalized in terms of the local profile scale $L_\perp/c_s$. The parameters $\hat{\beta} = (4\pi n T_e/B^2)(qR/L_\perp)^2$, $\omega_n = L_\perp/|\nabla \ln n|$ and $\hat{\mu} = m_e/M_i(qR/L_\perp)^2$ are constants. Numerically, we use a second order upwind finite-difference scheme [72]. Initialization of the simulation is through a density fluctuation amplitude well above unity which is driven nonlinearly [8] and then relaxes to a steady turbulent state. Static radial electric fields and associated velocity shear are not included in our simulations, as they only represent another free parameter that has to be put in by hand: turbulence alone is not effective in spinning the shear flow up to substantial amplitude [72].

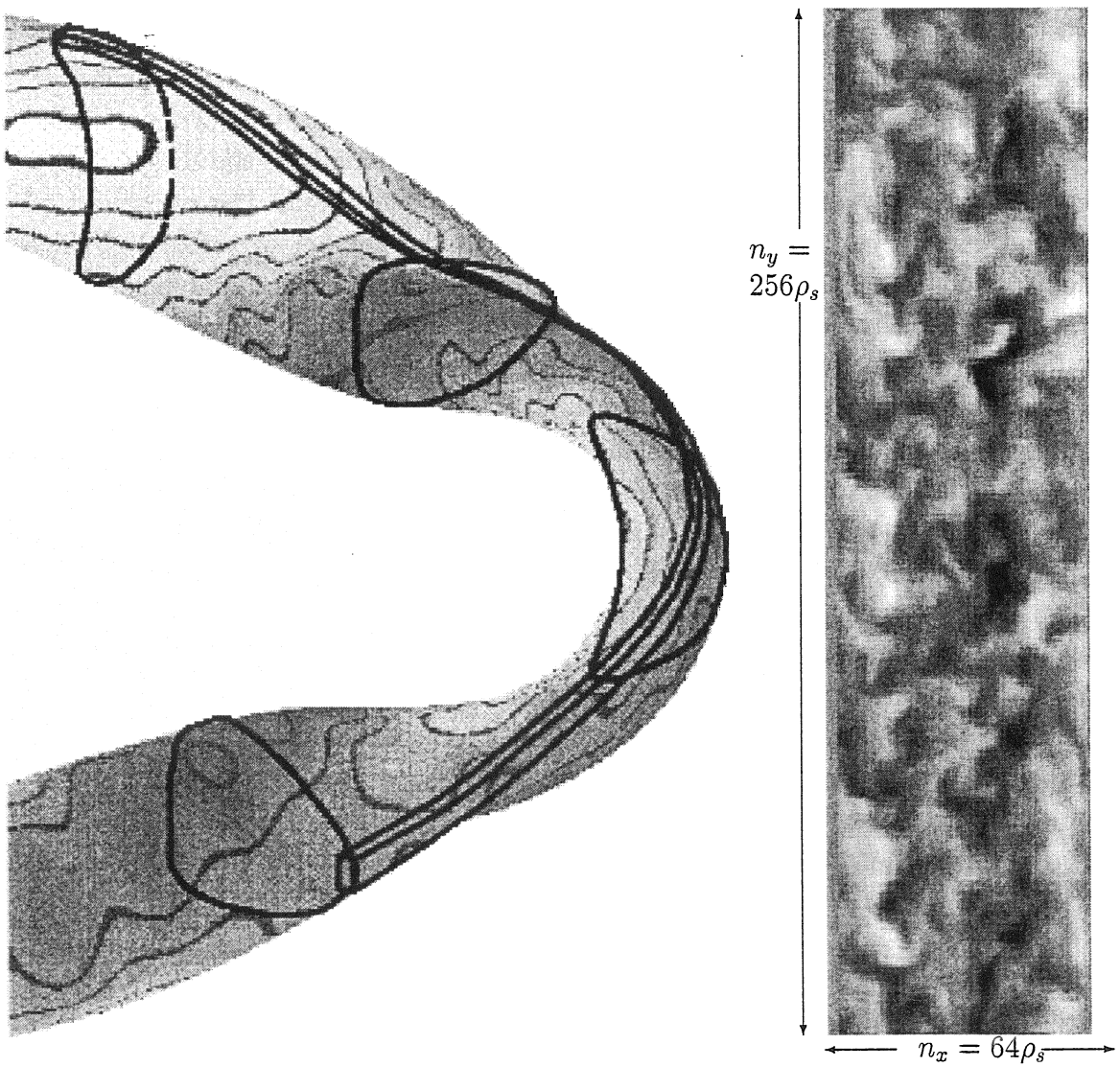

Figure 6.1. *Part of a flux tube (left) and poloidal cut of simulated density fluctuation for expected edge parameters in Wendelstein 7-X (in original size, right).*

6.2 Flux tube representation of stellarator geometry

Local alignment of the coordinate system to the magnetic field allows use of relatively few grid nodes in the parallel coordinate z: The grid size in our simulations was $64 \times 256 \times 64$ in (x, y, z) space with a computational poloidal domain in (x, y) of one ρ_s per grid node, what corresponds to about 4 cm $\times$ 16 cm for typical edge plasmas with drift scale $\rho_s = \sqrt{T_e M_i} c/eB$. An extension of the globally consistent flux tube model [73] from an axisymmetric tokamak to a stellarator is in principle straightforward, but not without fundamental obstacles. When in general the rotational transform ι is irrational, the flux tube will not close in on itself. The code DALF3, which we use, solves this problem by aligning the flux tube in a local approximation centrally around a rational field line and corrects deformation in the perpendicular plane caused by finite shear with an appropriate shear shift transformation. In a tokamak, this approach is appropriate even for a high rational ratio $\iota = m/n$, as the geometric background properties only depend on the poloidal angle θ, regardless of the number of toroidal circuits until field line closure. In a stellarator, however, the axisymmetry is broken and helical variations of the metric become significant. The variations of background geometry along the field line scale with the number of toroidal circuits and field periods N_f, and so does the number of necessary parallel grid points. For arbitrary rotational transform, the number of grid points evidently diverges rapidly. Thus, for future quantitative simulations of stellarator turbulence, a 3D hollow flux cylinder model will have to be developed instead of the present flux tube approach. For our current purpose of qualitative identification of the relevant geometrical quantities that determine drift wave turbulence in stellarators, we can take advantage of the fact that the edge rotational transform of advanced stellarators like *Wendelstein 7-X* is near unity: $\iota(\Psi_0) = 0.98 \approx 1$ on the last closed flux surface Ψ_0. Of course, the surface with $\iota \equiv 1$ is governed by generic island formation of the five-period Helias. When we nevertheless assume a rotational transform of unity for the start, we hence do not map the geometrical properties of *Wendelstein 7-X* or any other specific configuration exactly, but still gain a quite accurate model of Helias type geometry.

From local flux tube coordinates $x^i \in (x, y, z)$, metric elements $g^{ij} = \nabla x^i \cdot \nabla x^j$ are obtained. They are closely related to Hamada coordinates (i.e. unit Jacobian flux coordinates) as outlined in chapter 2 via

$$g^{xx} = (1/4s) g^{ss}, \quad g^{xy} = (1/2) g^{s\alpha} \quad \text{and} \quad g^{yy} = s g^{\alpha\alpha}. \tag{6.11}$$

All geometric quantities are assumed to depend only on z and to be constant on the xy domain. The magnetic field takes on the particularly simple form $\mathbf{B} = B_0 \nabla x \times \nabla y$. In this representation the perpendicular Laplacian becomes

$$\nabla_\perp^2 = \nabla \cdot \nabla_\perp = g^{xx} \partial_x^2 + 2 g^{xy} \partial_{x,y}^2 + g^{yy} \partial_y^2. \tag{6.12}$$

The curvature operator $\mathcal{K} = \mathcal{K}^x \partial_x + \mathcal{K}^y \partial_y$ is expressed in terms of geodesic curvature

$$\kappa_G = \nabla\alpha \cdot \nabla \ln B - \Lambda \kappa_N, \tag{6.13}$$

normal curvature

$$\kappa_N = \nabla s \cdot \nabla \ln B \tag{6.14}$$

and $\Lambda = g^{s\alpha}/g^{ss}$ is the local shear integrated along a field line. In detail we get

$$\begin{aligned} \mathcal{K}^x &= -\frac{(L_\perp/a_0)}{B^2}\left[\mathbf{B} \times \nabla \ln B^2\right] \cdot \nabla x \\ &= -\frac{(L_\perp/a_0)}{2\sqrt{s}\hat{B}}\left[(\nabla s \times \nabla\alpha) \times \nabla \ln B\right] \cdot \nabla s = \frac{(L_\perp/a_0)}{2\sqrt{s}\hat{B}} g^{ss}\kappa_G, \end{aligned} \tag{6.15}$$

$$\mathcal{K}^y = \frac{(L_\perp/a_0)}{\hat{B}}\sqrt{s}g^{ss}\left[\kappa_G\Lambda - \kappa_N(2\hat{B}/g^{ss})^2\right]. \tag{6.16}$$

Here $\hat{B} = B/B_0$ has been denoted. To avoid grid deformation, a shear shift is introduced into the metric: One choses $y_k = y - a_k(x)$ such that $g_k^{xy} = 0$ [72]. This is achieved by a shift $a_k(x) = x_k'$ and thus $a_k' = g^{xy}/g^{xx}$ evaluated at $z = z_k$. Also changed are $g_k^{yy} = g^{yy} - a_k' g^{xy}$ and $\mathcal{K}_k^y = \mathcal{K}^y - a_k'\mathcal{K}^x$.

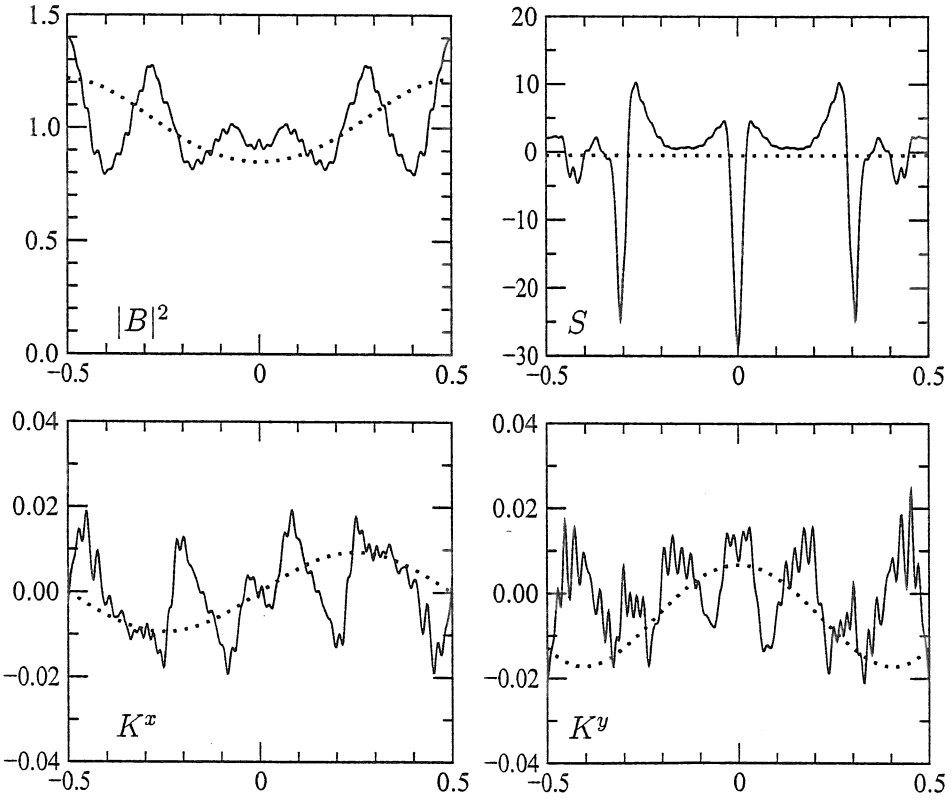

Figure 6.2. *$|B|^2$, local shear S and curvatures $\mathcal{K}^x$ and $\mathcal{K}^y$ along the field line $\alpha = 0$ for a tokamak (dotted lines) and Wendelstein 7-X (solid lines), each with $\iota \equiv 1$.*

6.3 The role of local magnetic shear in stellarator turbulence

We investigate the dependence on geometrical properties with an actual W7-X stellarator equilibrium, with a simple circular "tokamak", and with suitable interpolations between both: The metric is gradually varied by separately adding either local curvature or local shear properties to a tokamak configuration, corresponding to increased swelling in a toroidally modulated bumpy torus metric or increased ellipticity in a simple elliptic l=2 stellarator model, respectively. These transition metrics serve solely to highlight and separate the qualitative distinctions between tokamak and stellarator geometry; they need not represent actual MHD equilibria. For five field periods such configurations are shown in Fig. 6.3. Explicitly, the bumpy torus metric is obtained by modifying the small radius r of a (in lowest order circular) torus as $r(\varphi) = r_0 \cdot E_B = r_0 \cdot [1 + \epsilon_B \cdot \sin(N\varphi)]$, which has the effect of adding N deformations along toroidal angle φ of scale ϵ_B. From this we can obtain all metric elements and the magnetic field stregth. This configuration mimics for $0 \leq \epsilon_B \leq 0.3$ a smooth transition of curvature properties from a tokamak to a Helias stellarator. In the limit of a large aspect ratio ($A_0 \gg 1$) circular ($E_B = 1$) tokamak we regain the usual form $\hat{B} \approx 1 - A_0^{-1} \cos\eta$. Similarly, we can additionally model increasing local shear by defining an l=2 stellarator type metric with variable ($0 \leq \epsilon_l \leq 0.3$) ellipticity by $r(\eta, \varphi) = r_0 \cdot E_l = r_0 \cdot [1 - \epsilon_l \cdot \cos(2\eta + N\varphi)]$. For all configurations we assume the same W-7X-like parameters: aspect ratio $A_0 = 10.6$ and $\iota(s = 0.95) = 1$.

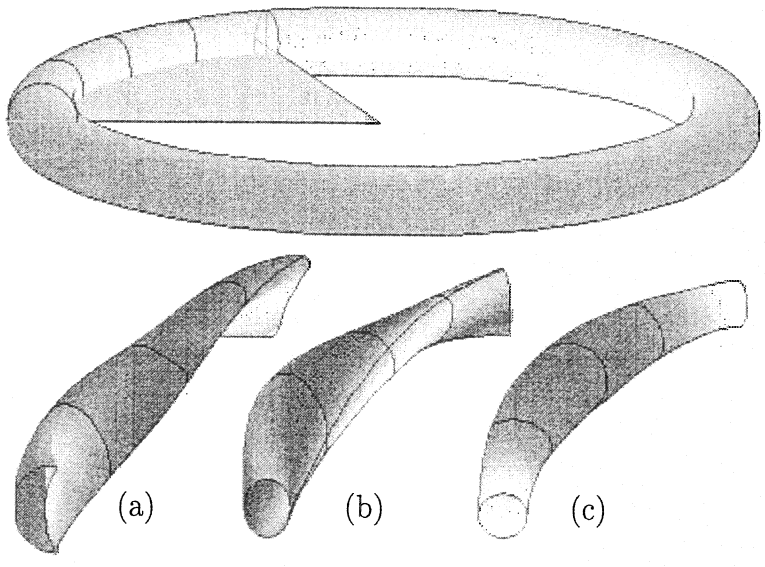

Figure 6.3. *A simple circular torus (top) is divided into five periods. The geometry of Wendelstein 7-X (a) is gradually approximated by metric models of a l=2 stellarator (b) and a bumpy tokamak (c). The elliptical elongation of case (b) leads to increased local shear, wheras (c) causes a modulation of curvature only.*

By contrast to the axisymmetric case, it is no longer true that one field line is representative for the whole flux surface. For N-fold toroidal symmetry, the field lines labeled $\alpha = \theta - \iota\zeta = i/N$ (with $\alpha \in [0...1]$) are identical for $i \in [0, 1, ..., N]$. To cover a fair proportion of the flux surface with a representative choice, simulations on four different field lines for $\alpha \in [0...1/N]$ with $N = 5$ are usually sufficient. For characterization of the turbulence level we will refer to the average fluctuation induced particle transport $\Gamma_n = \langle v^x_{E\times B} \cdot n \rangle$. In Fig. 6.5 (bold line) we show the dependence $\Gamma_n(\alpha)$ on the field line label for W7-X. Depending on α, we observe a significant inhomogeneity of fluctuation amplitude and transport, with Γ_n minimal for $\alpha = 0$.

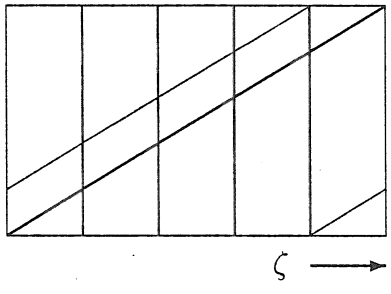

Figure 6.4. *For $\iota = 1$, the thick ($\alpha = 0$) and thin ($\alpha = 0.2 \cdot 2\pi$) field lines in the ζ-θ plane are identical with respect to their geometric properties for the five-fold toroidal symmetry of a Helias stellarator.*

This difference in the level of turbulence becomes clear, when all relevant geometric quantities along the field lines are examined. Most obvious is the perpendicular variation of normalized local shear $S(\zeta, \alpha) = (2s/\iota)\partial_\zeta \Lambda$ along the field lines. Comparison of the inverse field-line averaged absolute value of local shear (dotted line in Fig. 6.5) with the level of turbulence clearly suggest a suppression of transport on field lines with large average absolute local shear. The local shear signature $S(\zeta)$ of W7-X along the different field lines shows three-fold pronounced maxima on the field line for least fluctuations, whereas the most turbulent field line shows only two, less pronounced maxima. For $|B|$, $\mathcal{K}^x$ and $\mathcal{K}^y$ no such significant dependence is evident. For both model metrics there is much less variation with α compared to W7-X both in the metric and in the turbulence.

Such an effective localization of turbulence due to local shear properties has not yet been observed experimentally. There may be serveral reasons: At first, our assumption of $\iota = 1$ is somewhat artificial. In reality, $\iota(s{=}0.95) \approx 0.95$ is not necessarily rational in W7-X, and a field line does not connect to itself after a finite number of toroidal circuits. The usually long parallel wavelenghts can thus connect regions of low and high local shear and average out the transport levels. Also our treatment of the metric is local in x and y directions. A nonlocal metric in perpendicular direction y may couple the fluctuations for different field lines and also smooth the difference in amplitudes out

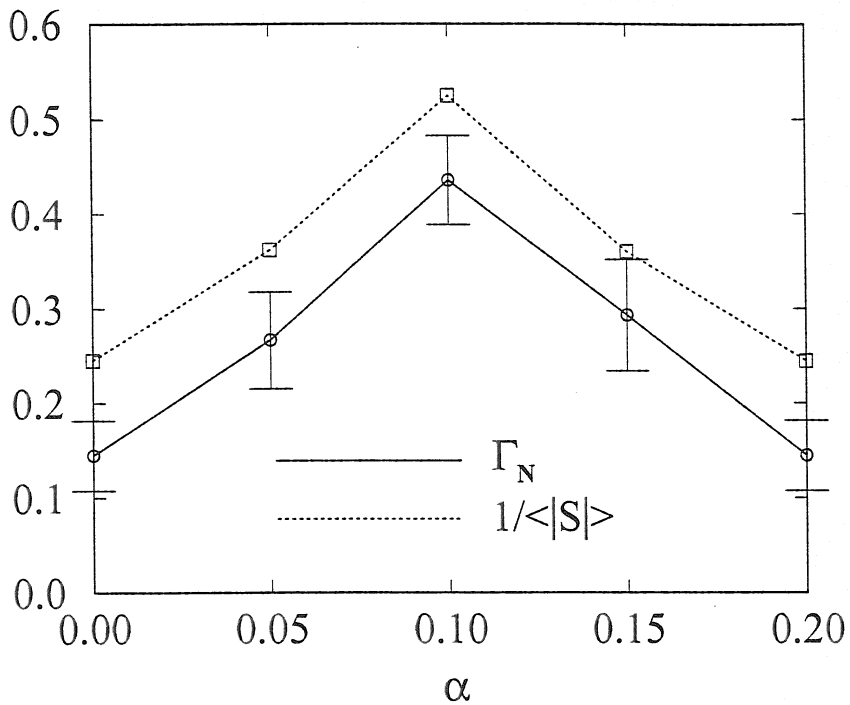

Figure 6.5. *Calculated transport $\Gamma_n(\alpha)$ can be directly related to the mean absolute local shear in the computational domain.*

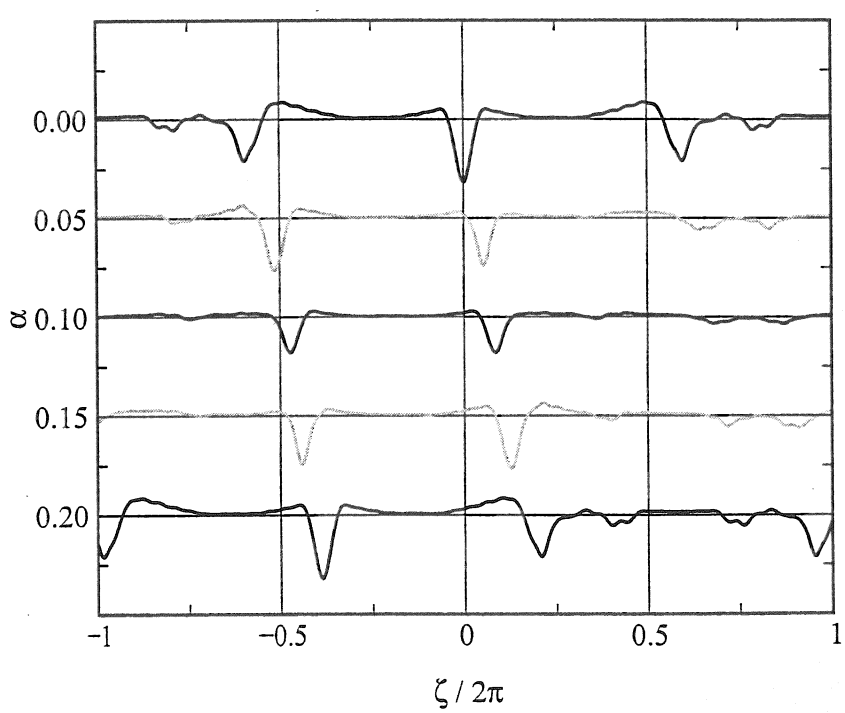

Figure 6.6. *Local shear $S(\eta)$ along $\alpha = 0$, $\alpha = 0.2 \cdot 2\pi$ and three intermediate field lines.*

to an average value, making the inhomogeneity significant only for large drift ratios $\delta = \rho_s/a_0$. Further, a poloidal rotation of the plasma, which has been neglected in our calculations, may also have a similar effect by connecting regions of different local shear. And finally, most present stellarator experiments operate with fixed diagnostic locations, and a scan in poloidal directions on the relevant scales has to our knowledge not been performed before. Nevertheless, the main point of our results is that they point to the average over the full flux surface of the absolute local shear as a general replacement for global shear in the overall dissipative effect on drift wave turbulence.

6.4 Transition from tokamak to stellarator turbulence

In addition it is possible to smoothly vary the model metrics by changing ϵ, that had up to now been fixed to $\epsilon = 0.2$. A change from 0 to 0.3 on the field line $\alpha = 0$ shows in Fig. 6.8 a continous decrease of turbulent transport for the l=2 metric with ϵ, which can also be attributed to the increase of local shear for more pronounced elongation. In case of the bumpy torus, no change is observed up to an $\epsilon_B = 0.2$. For still larger swelling, the helical variation in curvature shortens the parallel connection length between regions of positive and negative phase shift $(n - \phi)$. This effectively decreases the catalytic drive of the drift wave instability, and leads to a reduction of turbulence amplitude.

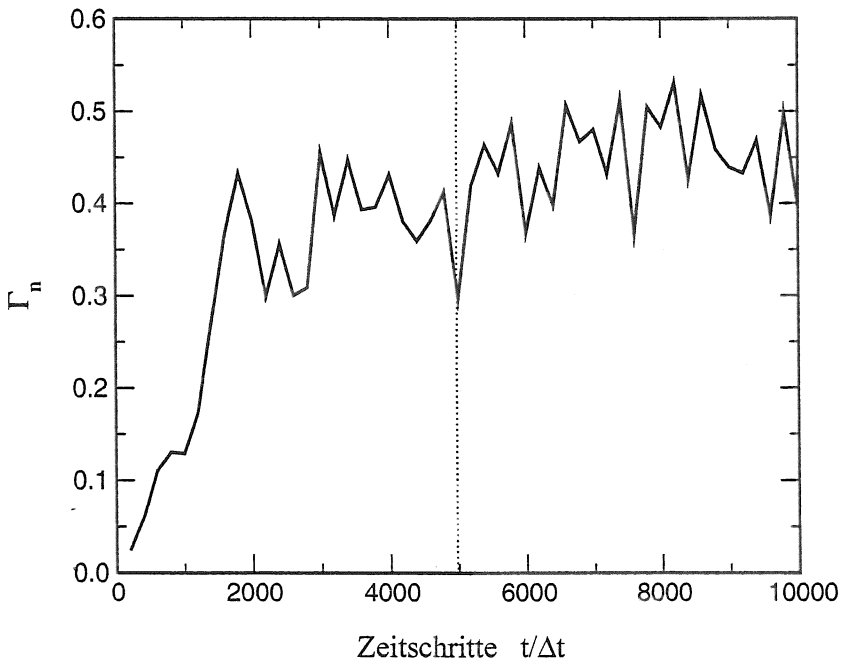

Figure 6.7. *Error bars stem from time averaging of quantities (here $\Gamma_n(t)$) during saturated turbulent state in the second half of the shown computation (values are printed out only after each 200th time step).*

One has to keep in mind that the values depicted in Figs. 6.5 and 6.8 are time averages during turbulent steady state with a statistical uncertainty $\Delta\Gamma_n/\Gamma_n \approx 10\%$ (see standard deviation error bars). A comparison of the density fluctuation spectra $E_n(k_y)$ in the Fig. 6.8 inset shows, despite the differences in amplitudes and transport as seen above, a high degree of similarity between the various geometries. This seems to confirm an empirical similarity for measured fluctuations in different experimental devices as found by Pedrosa *et al.* [69], in their case for frequency spectra after introduction of a device specific, frequency dependent scaling factor called λ.

From our simulations we conclude that this scaling factor is independent from the geometry of the different experiments. As other causes for the variation of λ we rather suggest device specific plasma parameters and differences in poloidal plasma rotation and velocity shear profiles. These have not yet been included in our simulations.

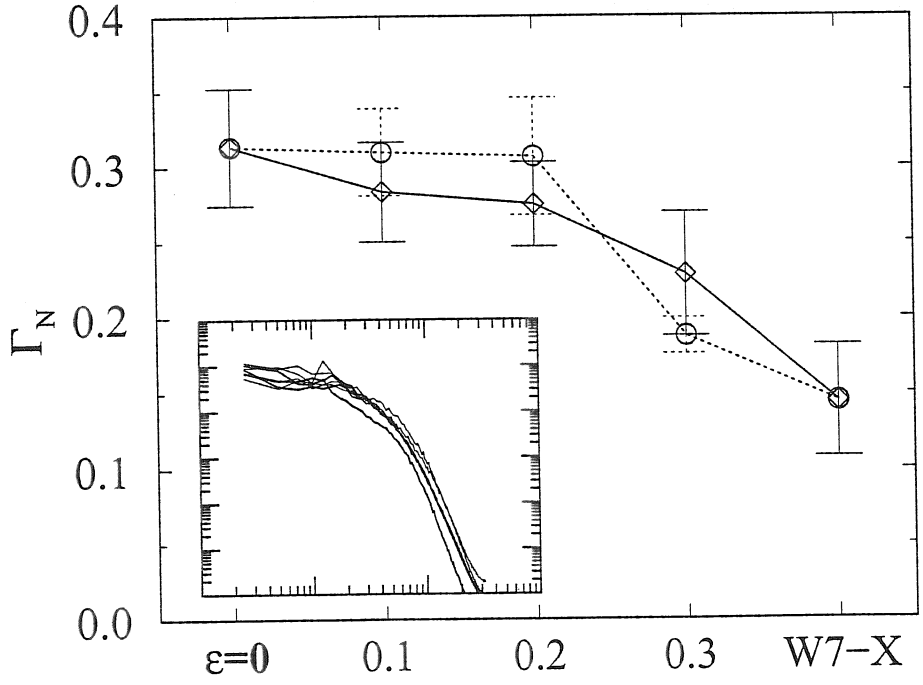

Figure 6.8. *Decrease of the turbulent transport through a transition from circular magnetic field geometry ($\epsilon = 0$) towards Wendelstein 7-X configuration via an l=2 stellarator (solid line) and bumpy torus metric (dotted). Inset: Note that wave number spectra $E_n(k_y)$ for the various configurations show a high degree of similarity despite the quite different transport levels*

6.5 Zonal flow dynamics

As an intrinsic part of the turbulence dynamics zonal $E \times B$ flows are generated via Reynold stress by coupling of eddies to flows with both $k_y = 0$ and $k_{||} = 0$.

By a decorrelation of vortices and transfer of energy from eddies to the flow the turbulence amplitude is effectively lowered. For tokamak geometry the suppression effects have been shown to be a relevant part of the overall dynamics [74].

When zonal flows are switched off in computations by setting the flux surface average Reynolds stress $\mathbf{v}_E \cdot \nabla \nabla_\perp^2 \phi$ set to zero, the level of transport was found to be higher by a factor of 2-5 in toroidal geometry [75].

For stellarator geometry ($\alpha = 0$) and otherwise same parameters as in Ref. [75], the damping effects are also clearly demonstrated in figure 6.9 over a range of various levels of collisionality $\hat{\nu}$.

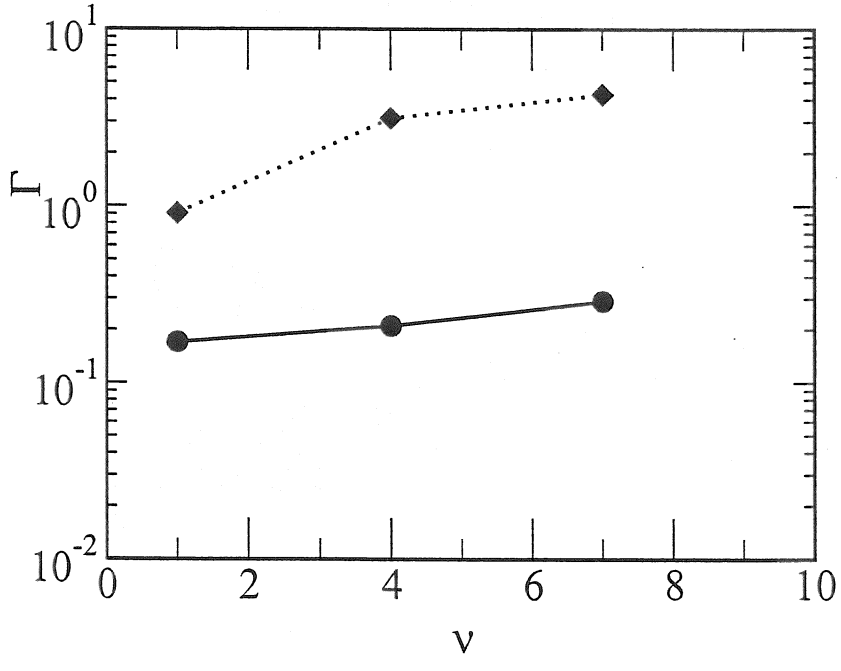

Figure 6.9. *The nominal transport Γ_n (dark line) for various collisionalities $\hat{\nu}$ in stellarator geometry is effectively lowered in comparison to the case with the flux surface averaged vorticity set to zero (dotted line). Zonal flows are, similar to the tokamak case, an essential part of the turbulence dynamics.*

6.6 Absence of helical ballooning

Linear drift wave theory in Helias geometry suggests, that the parallel structure of the mode is governed by a combination of helical and toroidal ballooning.

In our nonlinear turbulent simulations, however, no helical ballooning is observed. The drift wave structure limits itself to long parallel wavelengths, which average over the magnetic structure. We note especially a lack of asymmetry along the field line when the normal curvature departs from the simple sinusoidal form of a tokamak.

Fig. 6.10 shows minor variations in the turbulence amplitude along the field line, following more from the local shear than the normal curvature. Here the code parameters are set to more collisional tokamak-like resistive edge values because of the greater relevance of ballooning at these values ($\hat{\mu} = 5$, $\hat{\beta} = 1$, $\hat{\nu} = 4$, $\varepsilon = 18350$).

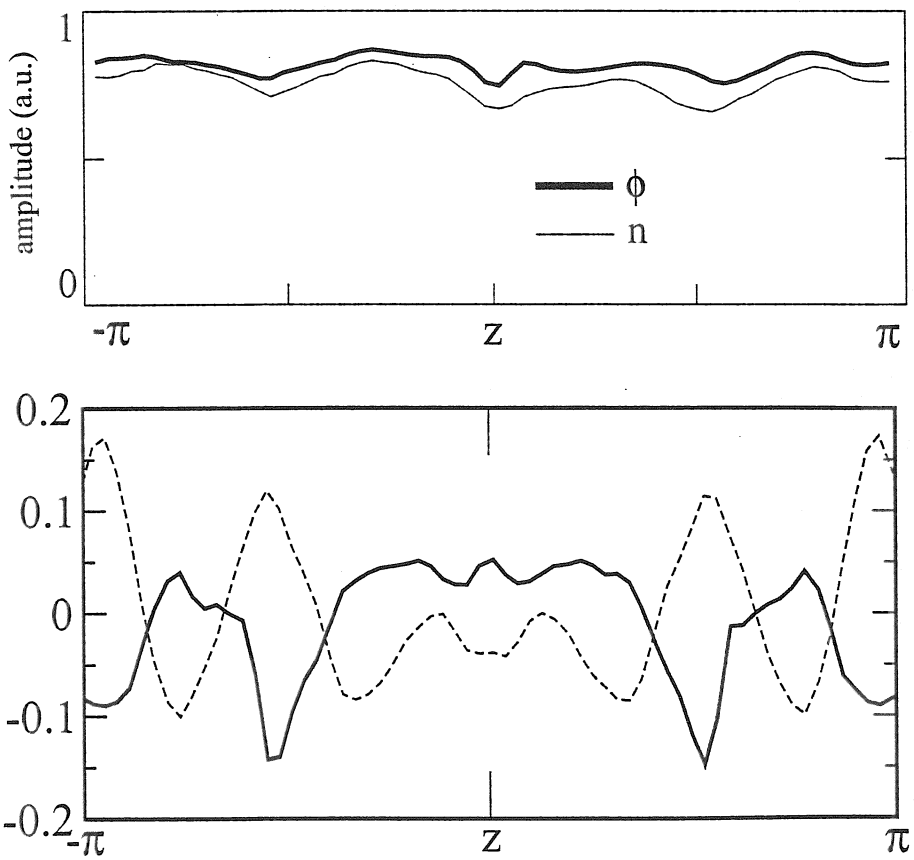

Figure 6.10. *Turbulence mode structure in a flux tube along z of potential and density fluctuations averaged over the perpendicular (x, y) plane (top), compared to $|B|$ (dotted line, bottom) and κ_N (solid line, bottom).*

6.7 Conclusions

Using direct numerical simulation of drift-Alfvén wave turbulence in actual stellarator geometry, we have shown that the local metric significantly influences turbulence amplitude and transport. Local shear was identified to play an important role in turbulence suppression and in effective localization of fluctuations on a flux surface. In contrast to the usual expectation that global shear is the more important quantity for drift wave stablity, we found that for situations of low global shear, the absolute local shear provides an effective substitute. Global shear is of course the average of the local shear, but the important quantity is apparently the average of the absolute local shear.

A stellarator allows, to some extent, for flexibility in design of the magnetic field structure. The existing Helias geometry is a result of optimization in MHD stability and neoclassical transport properties. Here local shear is found largest at the tips of triangular and elliptical shaped cross sections. The strong local deformations of the field geometry that alternate with more even regions arise as a side effect of the strategy to allow particle trapping mainly in regions with low field curvature. A minimization of turbulent "anomalous" transport may be achieved by explicitly accounting for a further increase of absolute local shear in the deformed regions, and for frequent penetration of a field line through these regions. The latter implies for example preference of a high number of field periods (e.g. 5 compared to 4) when the same total rotational transform is assumed. The quality of such a transport optimized configuration will then again have to be evaluated by means of numerical simulations.

Acknowledgements

Ceci n'est pas une pipe.
René Magritte[1]

I would especially like to thank

- H. Wobig for many useful discussions on the physics of stellarators and continous support of this work,
- B. Scott for making his tokamak edge turbulence codes `DALF3` and `GYRO` available to me and for lots of helpful discussions on drift waves, turbulence and much more,
- E. Strumberger and J. Kisslinger for providing the numerical Helias equilibria data,
- F. Jenko for useful discussions and benchmark efforts on the gyrokinetic code.

[1] "Dies ist keine Pfeife". Der Künstler Magritte wollte verdeutlichen, daß es sich nur um die *Abbildung* einer Pfeife handele. Manche grundlegende Eigenschaft des tatsächlichen Gegenstandes fehlt - so etwa kann man das Abbild sicherlich nicht rauchen. Doch auch dieses Abbild verhilft bereits, wesentliche Merkmale einer Pfeife zu vermitteln. Die Abbildung in der Einleitung dieser Arbeit, welche stark an eine Dreiecksebene der Flußflächen eines Stellarators erinnert, ist aus einem einfachen Algorithmus von M. Hénon für eine quadratische flächentreue Abbildung mit $p = -0.8$ erzeugt worden [76]. Derartige Abbildungsmethoden werden auch verwendet, um den Teilchentransport in einem Stellarator durch das Aufbrechen von Driftflächen zu simulieren. Siehe hierzu etwa Wobig und Kendl [24].

References

[1] Liewer PC 1985 *Nucl. Fusion* **25** 543
[2] Scott BD 1992 *Phys. Fluids B* **4** 2468
[3] Kick M, Maaßberg H, Anton M *et al.* 1999 *Plasma Phys. Controlled Fusion* **41** A549
[4] Dimits AM, Bateman G, Beer MA *et al.* 2000 *Phys. Plasmas* **7** 969
[5] Wobig H 1999 *Plasma Phys. Contr. Fusion* **41** A159
[6] Antonsen TM 1978 *Phys. Rev. Lett.* **41** 33
[7] Chen L, Guzdar PN, J.Y. Hsu JY, Kaw PK, Oberman C and White R 1979 *Nucl. Fusion* **19** 373
[8] Scott BD 1990 *Phys. Rev. Lett* **65** 3289
[9] Kendl A, Wobig H 1999 *Phys. Plasmas* **6** 4714
[10] Kendl A, Scott BD, Wobig H 2000 *Plasma Phys. Control. Fusion* **42** L23.
[11] Kendl A 2001 submitted to *Plasma Phys. Control. Fusion*
[12] Nührenberg J and Zille R 1986 *Phys. Lett. A* **114** 129
[13] Renner H, W7AS Team, NBI Group, ICF Group and ECRH Group 1989 *Plasma Phys. Controlled Fusion* **31** 1579
[14] Hartfuss HJ, Endler M, Erckmann V *et al.* 1994 *Plasma Phys. Controlled Fusion* **36** B17
[15] Hofmann JV, Baldzuhn J, Brakel R*et al.* 1996 *Plasma Phys. Controlled Fusion* **38** A193
[16] Beidler C, Grieger G, Herrnegger F *et al.* 1990 *Fusion Technol.* **17** 148
[17] Wobig H 1993 *Plasma Phys. Controlled Fusion* **35** 903
[18] Lotz W, Nührenberg J and Schwab C 1991 *Plasma Physics Control. Nucl. Fusion Res. 1990*, Vol. 2 (IAEA Vienna) 603
[19] Boozer AH 1997 *Plasma Phys. Reports* **23** 483
[20] D'haeseleer WD, Hitchon WNG, Callen JD and Shohet JL 1991 *Flux Coordinates and Magnetic Field Structure*, Springer (Berlin)
[21] Hirshman SP et al. 1986 *Comput. Phys. Commun.* **43** 143
[22] Nührenberg J and Zille R 1988 *in: Theory of Fusion Plasmas* (Proc. Joint Varenna-Lausanne Int. Workshop Varenna 1987) 3, Editrice Compositori, Bologna
[23] Dewar RL, Monticelli DA and Sy WNC 1984 *Phys. Fluids* **27** 1723

[24] Wobig H and Kendl A, 2000 *Controlled Fusion and Plasma Physics Proc. 27th Eur. Conf. (Budapest 2000)* vol 24 (Geneva: European Physical Society) P3.040
[25] Grulke O, Klinger T and Piel A 1999 *Phys. Plasmas* **6** 788
[26] Spatschek KH 1990 *Theoretische Plasmaphysik.* Teubner (Stuttgart)
[27] Mikhailovskii AB 1998 *Instabilities in an confined plasma.* Institute of Physics Publishing (Bristol)
[28] Braginskii SI 1965 *Reviews of Plasma Physics* I 203, Consultants Bureau (New York)
[29] Rutherford PH and Frieman EA 1968 *Phys. Fluids* **11** 569
[30] Taylor JB and Hastie RJ 1968 *Plasma Physics* **10** 479
[31] Moiseev SS and Sagdeev RZ 1963 *Soviet Phys-JETP* **17** 515
[32] Tsai ST, Perkins FW and Stix TH 1970 *Phys. Fluids* **13** 2108
[33] Hinton FL and Horton CW 1971 *Phys. Fluids* **14** 116
[34] Hirshman SP and Molvig K 1979 *Phys. Rev. Lett.* **42** 648
[35] Hasegawa A and Wakatani M 1983 *Phys. Rev. Lett.* **50** 682
[36] Horton W 1999 *Rev. Mod. Phys.* **71** 735
[37] Scott BD 1997 *Plasma Phys. Control. Fusion* **39** 1635
[38] Galeev AA, Oraevskii VN and Sagdeev RZ 1963 Sov. Phys.-JETP **17** 615
[39] Zeiler A, Biskamp D, Drake FF and Rogers BN 1998 *Phys. Plasmas* **5** 2654
[40] Pearlstein LD and Berk HL 1969 *Phys. Rev. Lett.* **23** 320
[41] Chen L, Chance MS and Cheng CZ 1980 *Nuclear Fusion* **20** 901
[42] Waltz RE and Boozer AH 1993 *Phys. Fluids B* **5** 2201
[43] Connor JW, Hastie RJ and Taylor JB 1978 *Phys. Rev. Lett.* **40** 396
[44] Antonsen TM and Lane B 1980 *Phys. Fluids* **23** 1205
[45] Dewar RL and Glasser AH 1983 *Phys. Fluids* **26** 3038
[46] Bhattacharjee A, Sedlak JE, Similon PL, Rosenbluth MN and Ross DW 1983 *Phys. Fluids* **26** 880
[47] Persson M, Lewandowski JLV, and Nordman H 1996 *Phys. Plasmas* **3** 3720
[48] Dominguez N, Carreras BA, Lynch VE and Diamond PH 1992 *Phys. Fluids* B 4 2894
[49] Lewandowski JLV 1997 *Phys. Plasmas* 4 4023
[50] Lewandowski JLV 1998 *Plasma Phys. Control. Fusion* 40 283
[51] Lewandowski JLV 2000 *Phys. Plasmas* **7** 3360
[52] Kleiber R 1999 IAEA Techn. Comm. Meeting, Kloster Seeon
[53] Lewandowski JLV 1997 *Can. J. Phys.* **75** 891
[54] Gladd NT and Horton WH 1973 *Phys. Fluids* **16** 879
[55] Bender CM and Berk SA 1978 *Advanced mathematical methods for scientists and engineers.* McGraw-Hill (New York)
[56] Stoer J and Bulirsch R (1980) *Introduction to numerical analysis.* Springer-Verlag (New York)

[57] Dewar RL and Hudson SR 1998 *Physica* D **112** 275
[58] Strumberger E, Wobig H, Kisslinger J, Nührenberg C. 1999 *Proc. 26th European Conf. on Contr. Fusion and Plasma Physics (Maastricht)*
[59] Tsang KT and Cheng CZ 1991 *Phys. Fluids B* **3** 688
[60] Kotschenreuther M, Rewoldt G and Tang WM 1995 *Comput. Phys. Commun.* **88** 128
[61] G.D. Smith 1978 *Numerical solution of partial differential equations: finite difference methods*, Clarendon Press (Oxford)
[62] Rewoldt G, Tang WM and Chance MS 1982 *Phys. Fluids* **25** 480
[63] Weiland J 2000 *Collective Modes in Inhomogeneous Plasma* (Institute of Physics Publishing, Bristol)
[64] Anderson J, Nordman H and Weiland J 2000 *Plasma Phys. Controlled Fusion* **42** 545
[65] Jenko F, Dorland W, Kotschenreuther M and Rogers BN 2000 *Phys. Plasmas* **7** 1904
[66] Kim JY and Wakatani M 1995 *Phys. Plasmas* **2** 1012
[67] Hatzky R 1999 IAEA Techn. Comm. Meeting, Kloster Seeon
[68] Stroth U 1998 *Plasma Phys. Control. Fusion* **40** 9
[69] Pedrosa MA, Hidalgo C, Carreras BA *et al.* 1999 *Phys. Rev. Lett* **82** 3621
[70] Burrell KH 1997 *Phys. Plasmas* 4 1499
[71] Boozer AH 1998 *Phys. Plasmas* **5** 1647
[72] Scott BD 2000 *Phys. Plasmas* **7** 1845
[73] Scott BD 1998 *Phys. Plasmas* **5** 2334
[74] Hahm TS, Beer M, Lin Z, Hammett G, Lee WW and Tang W 1999 Phys. Plasmas **6** 922
[75] Scott BD, Jenko F and Kendl A 2000 *Proc. 18th IAEA Fusion Energy Conference (Sorrento)*
[76] Lichtenberg AJ and Liebermann MA 1992 *Regular and chaotic dynamics.* Springer-Verlag (New York)